**Figure 4** Immunoelectron microscopy reveals partial colocalization of G37R SOD1 with chromogranins. Ultra-thin sections of spinal anterior horn from G37R *SOD1* mice (7 months old) were incubated with sheep polyclonal antibody to human SOD1 alone (top panels), or together with rabbit polyclonal antibody to CgA or CgB (lower left or right, respectively). For secondary antibody, we used 10-nm (top panels) or 5-nm (bottom panels) immunogold-conjugated anti-sheep IgG and 10-nm immunogold-conjugated anti-rabbit IgG antibodies. In rough ER, 10-nm clusters of immuno-gold particles were frequently detected (arrowheads). G37R SOD1 was occasionally detected in mitochondria (arrow, top-left), or in a vesicle (arrowhead, top-right) close to the plasma membrane (arrows, top-right). Double-staining revealed frequent 10-nm clusters of CgA or CgB (arrowheads, bottom left or right) and 5-nm gold particles (hSOD1, double arrowheads, bottom panels). Scale bars, 100 nm.
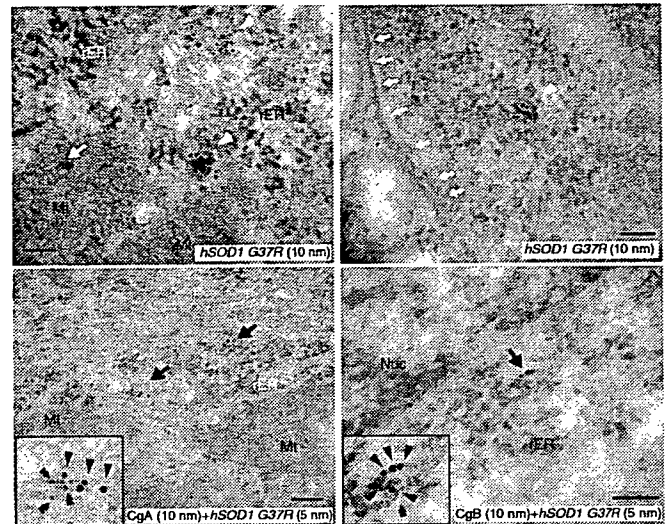
fractions, whereas only 2.61% of wild-type SOD1 accumulated there (**Fig. 3a**, bottom). Furthermore, G37R SOD1 but not wild-type SOD1 formed non-native dimers and high molecular aggregates in the membrane fractions in an age-dependent manner. To further clarify the distribution of mutant SOD1 in the transport vesicles, we performed sucrose density gradient ultracentrifugation of post-mitochondrial membrane fractions using spinal cord extract from presymptomatic G37R *SOD1* transgenic mice at 7 months old. Western blotting revealed that mutant SOD1 had a distribution pattern similar to chromogranins, the trans-Golgi marker adaptin-γ and the SNARE protein syntaxin-1, but different from the pattern of synaptophysin (**Fig. 3b**).

To further confirm the distribution of mutant SOD1 species in a secretory pathway, we purified TGN from the spinal cord lysates of *SOD1* (wild-type), G37R *SOD1* and G93A *SOD1* transgenic mice by an immuno-isolation technique using anti-TGN38 antibody bound to

protein G–coated magnetic beads. Anti-TGN38 is an affinity-purified polyclonal antibody specific to a 23-amino acid peptide corresponding to the cytosolic domain of rat and mouse TGN38 protein. Western analysis of the immunoprecipitates demonstrated that both G37R and G93A SOD1 co-precipitated with TGN38, indicating that mutant SOD1 is distributed in the TGN (**Fig. 3c**). Note that the wild-type SOD1 was also detectable in the TGN preparation, albeit at lower levels than mutant SOD1.

Further evidence for the specific interaction of CgA or CgB with mutant SOD1 proteins came from co-immunoprecipitation experiments using spinal cord lysates of transgenic mice. We found that rabbit polyclonal anti-CgA or anti-CgB antibody was able to pull down both G37R and G93A SOD1 mutants but not wild-type SOD1 (**Fig. 3d**). It should be noted that a non-native dimer of G37R SOD1 was more apparent than G93A SOD1 (double arrowhead), corresponding to the larger amount of co-immunoprecipitated G37R SOD1 than G93A SOD1.

To further investigate the distribution and colocalization of mutant SOD1 and chromogranins, we examined spinal cord sections from *SOD1* (wild-type) and G37R *SOD1* transgenic mice (7 months old) using immunoelectron microscopy. Mutant SOD1 protein was observed as small clusters of gold particles in the cytosol (**Supplementary Fig. 3** online), rough ER (arrowheads in **Fig. 4**, top-left), smooth ER and Golgi (**Supplementary Fig. 3**), and occasionally it was observed in mitochondria (arrow in **Fig. 4**, top-left) and transport vesicles (**Fig. 4**, top-right). Moreover, the double immunohistochemistry using secondary antibodies conjugated with different gold particles (5 nm or 10 nm) provided frequent detection of cluster complexes
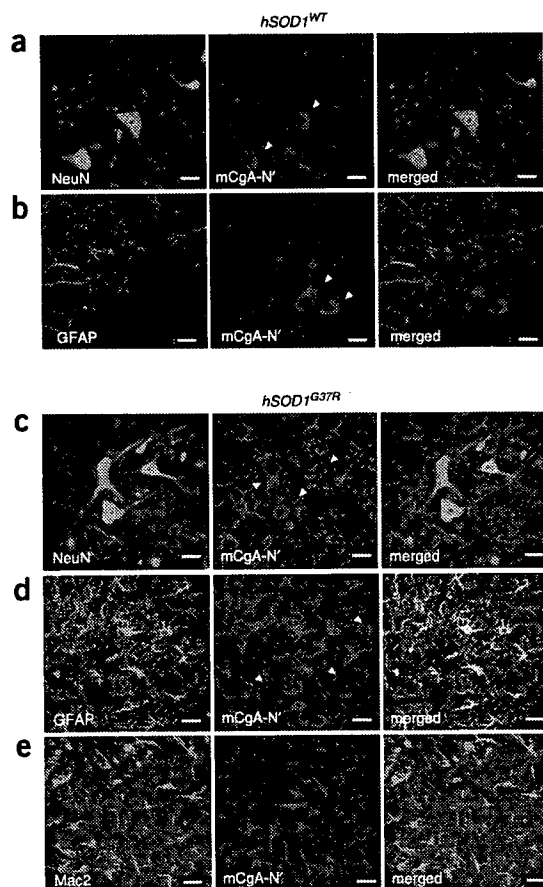
Figure 5 CgA is expressed in reactive astrocytes of spinal anterior horn from mutant *SOD1* transgenic mice. Double immunofluorescent experiments show the colocalization of CgA and GFAP in the spinal cord of transgenic mice carrying mutant *SOD1*, but not those carrying wild-type *SOD1*. (a,b) In wild-type *SOD1* mice, CgA was expressed only in the neurons labeled by anti-NeuN (a, mouse monoclonal), but not in reactive astrocytes labeled by anti-GFAP (b, mouse monoclonal). In G37R *SOD1* mice, in addition to the neuronal expression (c), CgA was also detected in reactive astrocytes (d), but not in the active microglial cells labeled by anti-Mac2 (e, rat monoclonal). Arrowheads and arrows, respectively, indicate neurons and astrocytes stained with anti-mCgA-N'. Left panels represent merged images from left and middle panels. Scale bars, 50 μm. Images show a representative sample from one of at least three independent experiments.

comprising SOD1 and chromogranins (**Fig. 4**; CgA bottom left, CgB bottom right). This colocalization was observed in rough ER, transport vesicles and granule-like structures. In contrast, wild-type SOD1 was chiefly located in the cytosol and occasionally in mitochondria and luminal structures including smooth and rough ER. The gold particles for wild-type human SOD1 tended to be singular or doublets, whereas clusters for G37R SOD comprised five to ten gold particles (**Supplementary Fig. 3**). No significant colocalization of wild-type SOD1 and chromogranins was detected. These findings confirm that mutant SOD1 can be recruited into the ER-Golgi pathway and interact with chromogranins.

Expression of CgA in reactive astrocytes in ALS mice

CgA is implicated in several neurodegenerative diseases including Alzheimer disease[21] and prion disease[22]. The N-terminal bioactive peptide of CgA, vasostatin, is implicated in microglial activation[24,32]. To investigate the distribution of proinflammatory fragments of CgA in the mutant *SOD1* transgenic mice, we raised a rabbit polyclonal antibody specific to the N-terminal peptide (16 amino acids) of the mature mouse CgA (anti-mCgA-N').

Western analysis showed that anti-mCgA-N' specifically recognized mouse CgA tagged by HA in the transfected COS-7 cells. Moreover, this antibody reacts with mouse CgA, but not with human CgA (**Supplementary Fig. 4** online). In transgenic mice overexpressing wild-type SOD1 (9 months old), immunofluorescence using anti-mCgA-N' showed CgA detection predominantly in neurons co-stained with anti-NeuN (**Fig. 5a**) and rarely in astrocytes labeled by antibody specific to glial fibrillary acidic protein (anti-GFAP; **Fig. 5b**). In contrast, prominent anti-mCgA-N' immunoreactivity was observed in reactive astrocytes of ventral horn in presymptomatic G37R *SOD1* mice (**Fig. 5c–e**, 8 months old) and G93A *SOD1* mice (**Supplementary Fig. 5** online, 80 d old). CgA also localized in neurons (**Fig. 5c**) but not in Mac2-labeled microglia (**Fig. 5e**) of G37R *SOD1* mice. Pre-incubation with the peptide antigen completely eliminated the signal (data not shown). These results suggest that CgA may be involved in the disease progression concomitant with astrocytosis.

CgA and CgB promote secretion of mutant SOD1

The combined microscopy and immunoprecipitation data presented above provide compelling evidence for the selective colocalization of
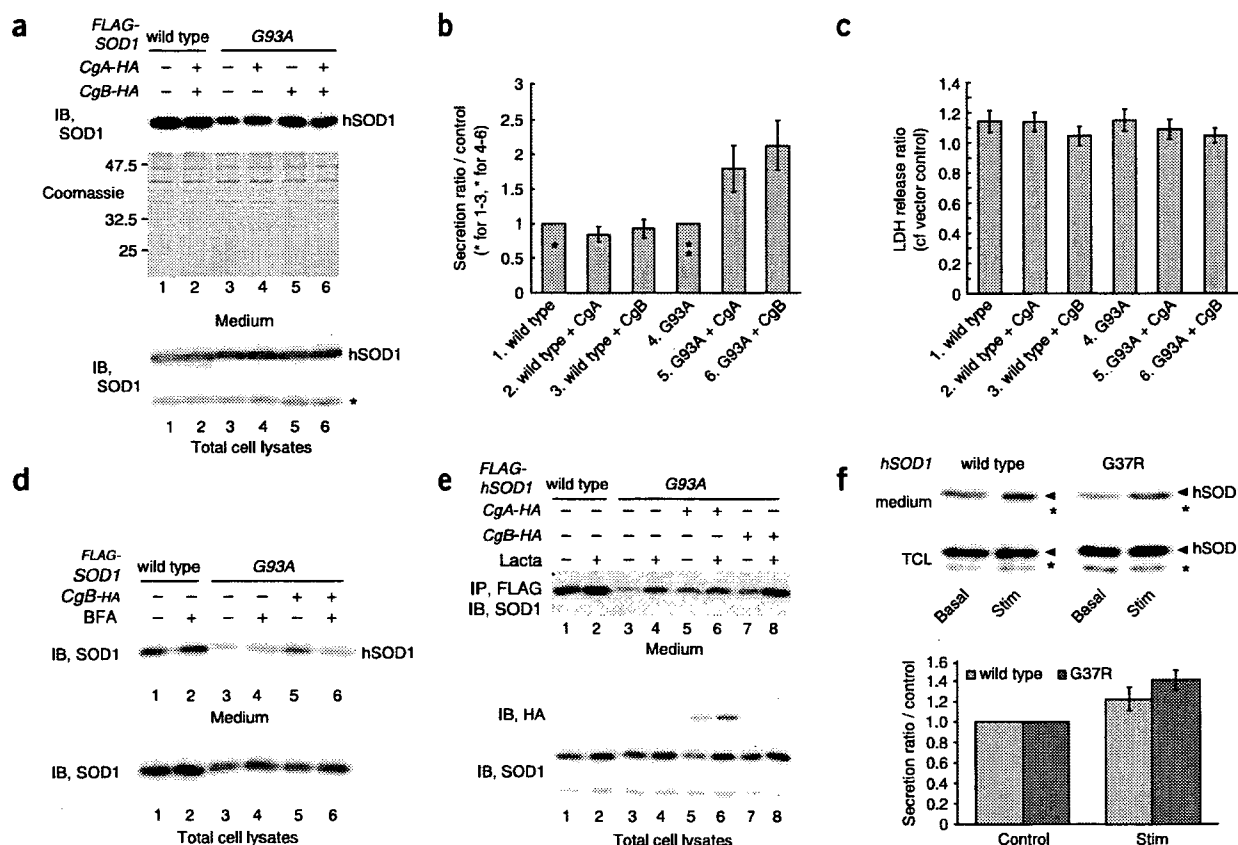

Figure 6 Chromogranins promote selective secretion of misfolded mutant SOD1. (a) CgA and CgB promoted specific secretion of mutant SOD1 in non-neurosecretory cells. COS-7 cells transfected with *FLAG-SOD1* (wild-type or G93A) and *CgA-HA* or *CgB-HA* were incubated in stimulation buffer. Medium was concentrated and analyzed by western blotting using SOD1-specific antibody. The SDS-PAGE gel was stained by Coomassie brilliant blue (Coomassie). Asterisk indicates endogenous SOD1. IB, immunoblot. (b) Densitometry of the secreted human SOD1 from the western blots. The values (mean ± s.e.m., $n = 3$) represent the ratio compared to control (lane 1 = control for wild-type (asterisk) and lane 4 = control for G93A SOD1 (double asterisks)). (c) LDH release assay demonstrating that transfection experiments did not provoke cell leakage. Medium was assayed 24 h after transfection. Value represents LDH release ratio compared with vector control (*pcDNA3*). Data are mean ± s.e.m. ($n = 3$). (d) Brefeldin A (BFA) inhibited chromogranin-mediated secretion of mutant SOD1. COS-7 cells transfected with FLAG-*SOD1* (wild-type or G93A) with or without CgB-HA were treated with 5 µM BFA for 1 h before exposure to stimulation buffer. (e) Effect of proteasomal inhibitor on mutant SOD1 secretion. Transfected NIH3T3 cells were treated with lactacystin for 20 h before the secretion assay. (f) Both wild-type and G37R SOD1 were secreted from embryonic spinal cord cultures from human SOD1 transgenic mice. Primary cultures were treated with basal or stimulation buffer for 15 min. Asterisks indicate endogenous mouse SOD1. Data given as ratio of secreted SOD1 from treated samples to that in basal-buffer samples (mean ± s.e.m., $n = 4$).
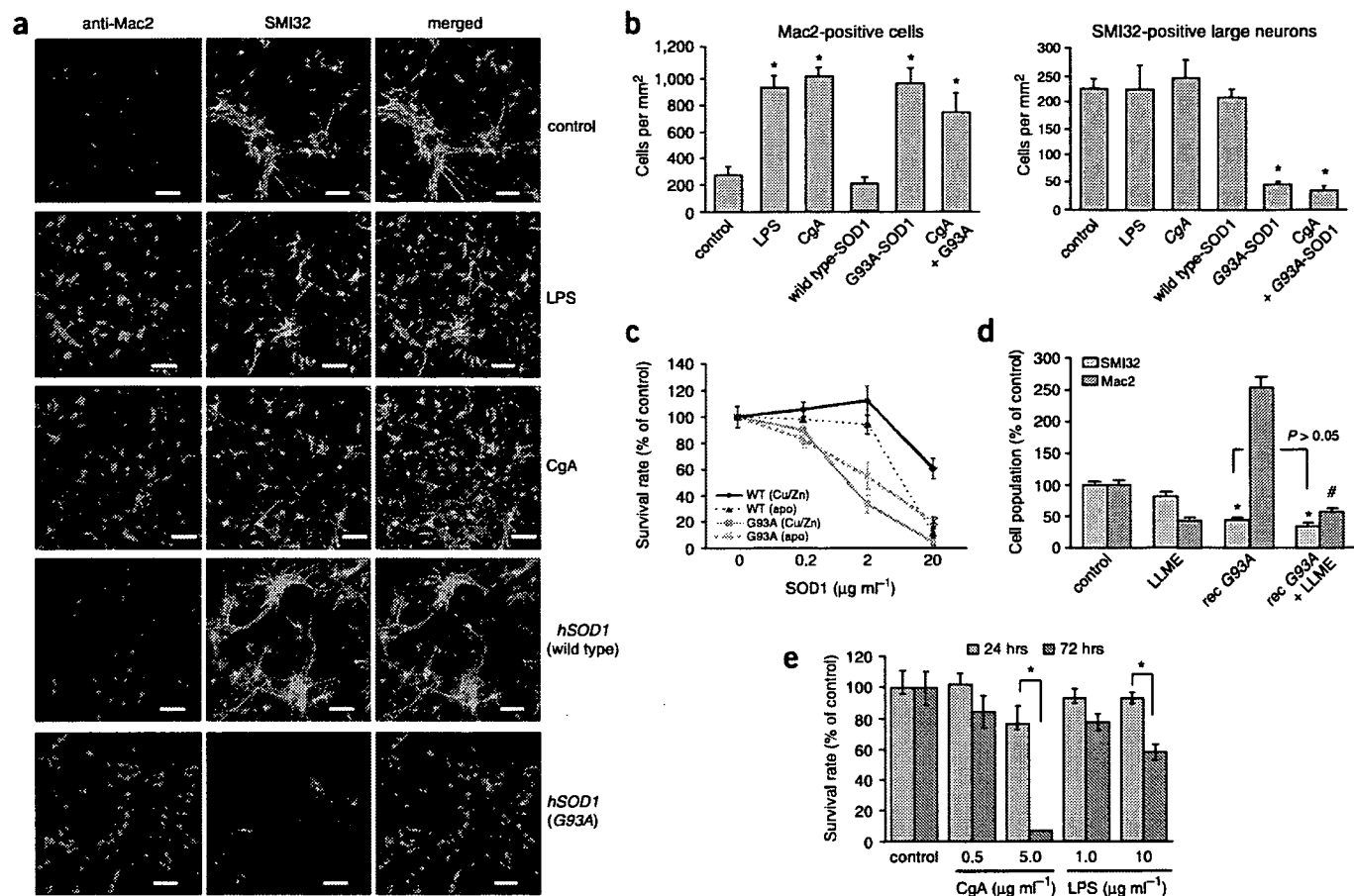
Figure 7 Activation of microglia by extracellular mutant SOD1. (a,b) Activation of microglial cell-line BV2 after treatment with conditioned medium from Neuro2a cells co-transfected with CgA and *SOD1* mutants (G85R or G93A). (a) RT-PCR study of TNF-α and GAPDH. For control, Neuro2a cells were treated with lipopolysaccharide (LPS). Notably, there was no microglial activation with medium from cells co-transfected with *CgA* and wild-type *SOD1*. Templates were examined at two different concentrations (1:10 diluted and original). (b) Each densitometric value was normalized with GAPDH and averaged from results of two different concentrations of templates. Each value represents a ratio compared to control lanes (bar 1 is the control for bar 2, and bar 3 is the control for 4–10), expressed as mean ± s.e.m. (c) Direct effect of mutant SOD1 on microglial activation. BV2 cells were treated with recombinant CgA (1 μg ml^{-1}), human SOD1 (wild-type or G93A, 2 μg ml^{-1} each) or LPS (10 μg ml^{-1}) as a positive control for 18 h, as shown in the bottom box. Semi-quantitative RT-PCR was performed in the same manner as in a. Each densitometric value was normalized by GAPDH and an expression ratio was obtained by comparison with control (bar 1 in each graph). The ratio was averaged from three experiments and expressed as mean ± s.e.m. *$P < 0.05$ versus sham treatment (lane 1). #$P < 0.05$ versus wild-type SOD1 treatment (lane 4) assessed by analysis of variance (ANOVA).

mutant SOD1 with chromogranins in mouse models of ALS. These results prompted us to investigate whether mutant SOD1 molecules were secreted together with chromogranins. We conducted secretion experiments using nongranular COS-7 cells that are lacking endogenous chromogranins[33]. Expression plasmids coding for FLAG-tagged SOD1 (wild-type or G93A mutant) and HA-tagged mouse CgA or CgB were transiently co-transfected in COS-7 cells. Both wild-type and G93A mutant SOD1 were detected by western analysis in the control medium after a 15-min incubation. Moreover, treatment with stimulation buffer containing 2-mM BaCl$_2$ and 50 mM KCl increased the amount of both wild-type and mutant SOD1 in the medium 1.2-fold compared with control buffer (data not shown). These data imply the existence of constitutive and regulatory secretory pathways for SOD1 in these cells. It is noteworthy that both CgA and CgB promoted secretion of G93A SOD1, whereas secretion of wild-type SOD1 was not affected by CgA or CgB (Fig. 6a,b). Judging from the amount of lactate dehydrogenase (LDH) released, the effects of chromogranins on secretion of mutant SOD1 did not result from cell death or membrane disintegration caused by overexpression (Fig. 6c). We also examined the effect of Brefeldin A (BFA) on SOD1 secretion to further address the involvement of the ER-Golgi network. In COS-7 cells, BFA did not reduce the secretion of either mutant or wild-type SOD1 in absence of CgB (Fig. 6d, lanes 2 and 5). BFA did, however, inhibit the CgB-mediated secretion of mutant SOD1 (Fig. 6d, lanes 7 and 8). This suggests that CgB contributes to the secretion of mutant SOD1 proteins through the TGN. We conclude that chromogranins promote the secretion of mutant SOD1, but not of wild-type SOD1.

Proteasome inhibition enhances secretion of mutant SOD1

Because previous studies showed an impairment of proteasomal activity in cells expressing mutant SOD1[11], we examined the effect of a proteasome inhibitor on the secretion of human SOD1 species in non-granular NIH3T3 cells. The treatment of transfected NIH3T3 cells with a specific proteasome inhibitor, lactacystin (5 μM), enhanced the secretion of mutant SOD1 in the presence or absence of chromogranins (Fig. 6e).

SOD1 secretion from spinal cultures of SOD1 mouse embryo

Both wild-type and mutant SOD1 have been detected in the cerebrospinal fluid (CSF) of *SOD1* transgenic rats[34] and humans carrying a

SOD1 mutation[35]. However, it is technically difficult to prove this finding in mice, because of the small space for CSF with high occurrence of contamination from the blood or tissues. We carried out spinal cord cultures from *SOD1* transgenic mice to confirm that SOD1 can be secreted. Spinal cord cultures were prepared from E13 embryos and then analyzed after 14 d *in vitro*. Secretion analysis of the culture medium revealed that both wild-type and G37R SOD1 can be detected in basal secretion buffer. Exposure of the cells to stimulation buffer containing BaCl$_2$ (2 mM) and KCl (50 mM) for 15 min promoted the secretion of both wild-type and G37R SOD1, but more robustly in G37R (Fig. 6f). This result indicates that SOD1 can be secreted in both a constitutive and regulated manner.

Extracellular SOD1 mutants cause microgliosis and neuron death

There is evidence for involvement of CgA in microglial activation[32]. To examine the effects of secreted mutant SOD1 together with CgA on microglial activation, we treated BV2 microglial cells with conditioned medium from Neuro2a cells that were transfected with various human *SOD1* species (wild-type, G85R and G93A), with or without CgA. Semi-quantitative reverse-transcriptase PCR (RT-PCR) was performed using total RNA from BV2 cells to monitor expression of mRNA for proinflammatory molecules. RT-PCR results showed that the combination of mutant SOD1 and CgA resulted in a medium that induced TNF-α expression in BV2 cells (Fig. 7a,b).

To investigate whether extracellular SOD1 mutants activate microglia, we exposed the BV2 cells to recombinant human SOD1 or CgA (extracellular) to determine whether microglial activation was mediated directly by these molecules. The results showed that extracellular mutant G93A SOD1 with or without CgA induced BV2 cells to produce TNF-α, cyclooxygenase-2 (COX-2) and inducible nitric oxide synthase (iNOS) (Fig. 7c). In contrast to mutant SOD1, the recombinant wild-type SOD1 caused suppression of microglial activation, which is in agreement with a protective role for secreted wild-type SOD1 as recently suggested[35].

We further investigated the effects of extracellular SOD1 (wild-type and G93A) and CgA proteins using primary spinal cord cultures derived from E13 mouse embryos. Spinal cord cultures at 14 d after plating were exposed to these recombinant proteins or to lipopolysaccharide (LPS) for 24 h. Treatment of the cultures with CgA and/or

Figure 8 Extracellular SOD1 mutant triggers microgliosis and motor neuron death. (a) Immunofluorescence images of primary spinal cultures doubly stained by anti-Mac2 antibody and SMI32. Scale bars, 50 μm. (b) Extracellular SOD1 mutant activated microglia and killed motor neurons of embryonic spinal cord cultures. Spinal cord cultures were treated with lipopolysaccharide (LPS, 10 μg ml^{-1}), recombinant mouse CgA (5 μg ml^{-1}) or recombinant SOD1 (wild-type or G93A, 2 μg ml^{-1}) for 24 h. Cultures were fixed with 4% paraformaldehyde and doubly labeled with antibody to Mac2 (top) or antibody to the nonphosphorylated neurofilament NFH (SMI32) (bottom). The number of labeled cells at eight different areas from two sister cultures were averaged and expressed as cells per mm^2. Values indicate mean ± s.e.m. ($n = 8$). *$P < 0.01$ versus controls. (c) Dose-dependent toxicity of G93A and wild-type SOD1 in holo- or apo-states to spinal cord cultures. Spinal cultures were exposed to metal-deficient (apo) or metallated (Cu/Zn) recombinant G93A SOD1 or wild-type SOD1 for 24 h. Values indicate mean ± s.e.m. ($n = 8$). (d) Elimination of microglia did not affect extracellular SOD1-induced motor neuron death. Cultures were pre-treated with LLME (5 mM) for 16 h before application of recombinant G93A SOD1 (2 μg ml^{-1}) for 24 h. Values indicate percent survival compared with control culture (mean ± s.e.m., $n = 8$–24). *$P < 0.01$ versus control, #$P < 0.01$ versus recombinant G93A treatment. (e) Motor neuron death caused by longer time exposure to CgA. Spinal cultures were exposed to CgA or LPS for 72 h or 24 h. Values indicate mean ± s.e.m. ($n = 8$). *$P < 0.01$.

G93A SOD1 significantly increased the number of active microglia, like LPS treatment, as determined with antibody specific to Mac2 (Fig. 8a and top graph in Fig. 8b). On the other hand, whereas exposure to extracellular CgA (5 μg ml^{-1}) or LPS (10 μg ml^{-1}) for 24 h did not affect the number of motor neurons stained with SMI32 (an antibody that labels unphosphorylated neurofilament-H), recombinant SOD1 mutant (2 μg ml^{-1}) caused massive neuronal death (bottom row in Fig. 8a and bottom graph in Fig. 8b). Thus, both CgA and mutant SOD1 were capable of activating microglia, but only mutant SOD1 was neurotoxic after a 24-h exposure. This toxicity is not related to the metal content, as the apo G93A mutant also exhibited toxicity to motor neurons (Fig. 8c). Notably, the apo form of wild-type SOD1 acquired some toxicity at 20 μg ml^{-1} when compared to holo-state wild-type SOD1 (Fig. 8c). Furthermore, we investigated the role of microglia in extracellular mutant SOD1-induced motor neuron death by eliminating microglia with exposure to leu-leu methyl ester (LLME), a lysosomotropic agent that kills actively phagocytic cells such as microglia[36]. Treatment of spinal

cultures with 5-mM LLME killed approximately 60–70% of Mac2-positive cells; control cultures showed only mild neurotoxicity (Fig. 8d). Pretreatment of the cell cultures with LLME did not rescue motor neurons from the toxicity of recombinant SOD1. Although these results indicate that extracellular SOD1 mutant can injure motor neurons independently of microglial activation, the role of microgliosis in motor neuron death cannot be excluded. The viability of motor neurons was affected by extracellular CgA or LPS after longer time exposures (Fig. 8e).

DISCUSSION

From the data presented here, we propose a novel pathogenic mechanism for ALS based on chromogranin-mediated secretion of misfolded SOD1 mutants (Supplementary Fig. 6 online). This model is supported by the following findings: (i) chromogranins interact with ALS-linked SOD1 mutants but not with wild-type SOD1, (ii) chromogranins can promote selective secretion of mutant SOD1, (iii) mutant SOD1 is distributed in the TGN, (iv) extracellular mutant SOD1 can

trigger microgliosis and neuronal death and (v) CgA expression is induced in reactive astrocytes.

It is unclear how the mutant SOD1 proteins are being recruited in the ER-Golgi secretory granule pathway to interact with chromogranins. SOD1 protein has no signal sequence. It is possible that an increased hydrophobicity of mutant SOD1 underlies its translocation in the ER-Golgi pathway, as reported for fibroblast growth factor-16 (ref. 37). The cytosolic soluble protein SOD1 normally maintains its hydrophilicity through intramolecular disulfide bonds. However, mutant SOD1 proteins are readily monomerized by a reducing environment[38], resulting in exposure of hydrophobic regions that can be recognized by Hsp proteins[16]. Once recruited into the ER-Golgi system, it is plausible that oxidative conditions might promote the formation of oligomers, as detected in **Figure 3a**. Our findings are consistent with a previous report that mutant SOD1, but not wild-type SOD1, can induce ER stress when transfected into COS-7 cells, with accumulation of mutant SOD1 in or on the ER[39]. Although we cannot exclude the possibility of a gain of toxic function due to ER stress, our data demonstrate that secretion of mutant SOD1 may represent a toxic pathway which would be in line with the non-cell-autonomous nature of ALS[14].

It is still unclear how mutant SOD1 associates with chromogranins in the ER-Golgi network. The results from our yeast two-hybrid interaction studies support a direct association. Moreover, *in vitro* binding of recombinant CgA with mutant SOD1, but not with wild-type SOD1, was also confirmed (data not shown). The presence of Hsp70-like motifs in both CgB and CgA may explain why chromogranins interact with mutant forms of SOD1, but not with wild-type SOD1. Mutant SOD1 proteins are known to show altered solubility and interact with heat shock/stress proteins[15,16].

Previous studies have shown that wild-type SOD1 can be secreted from cultured astrocytes[40] or thymus-derived cells[41]. Moreover, it has been reported that both wild-type and mutant SOD1 species are detected in the cerebrospinal fluid of both transgenic rats[34] carrying human SOD1 and ALS patients with the SOD1 mutation[35]. Our data together with these observations support the idea that both wild-type and mutant SOD1 proteins may be secreted through non-classical secretory pathways[42]. In addition, we propose a chaperone-like function for chromogranins in mediating the selective secretion of misfolded SOD1 mutants through the ER-Golgi network. In a recent study[35] with NSC34 cells, the secretion was interpreted as being beneficial because the extrusion of mutant SOD1 attenuated formation of toxic intracellular inclusions, ameliorating cell survival. That study did not, however, consider the presence of glial cells in motor neuron environment *in vivo* or the possibility that the disease in not strictly cell autonomous[14]. Conversely, we posit that secretion of mutant SOD1 mediated by chromogranins is deleterious because extracellular mutant SOD1 proteins caused microgliosis and death of embryonic motor neurons in mixed cultures (**Fig. 8**). Unlike secreted mutant SOD1, extracellular wild-type SOD1 probably has protective properties. Our data suggest that extracellular wild-type SOD1 suppresses extracellular inflammation, perhaps through an antioxidant effect (**Fig. 7c**), which would be consistent with the finding that intraspinal infusion of exogenous wild-type SOD1 in G93A SOD1 transgenic rats prolonged their lifespan[34].

From our *in situ* hybridization data and immunohistochemistry of spinal cord samples, it seems that chromogranin expression is elevated in both motor neurons and interneurons (**Supplementary Fig. 2**). Therefore, as depicted in our proposed pathogenic scheme (**Supplementary Fig. 6**), we view interneurons as important contributors to the secretion of chromogranins and mutant SOD1 complexes in the vicinity of motor neurons. In this model, it is the burden of extracellular mutant SOD1 in close proximity to motor neurons that would increase the risk of damage. Even though interneurons and motor neurons themselves would be the predominant source of extracellular mutant SOD1 mediated by chromogranin interactions, mutant SOD1 secreted by other pathways from other cells such as microglia and astrocytes could also contribute to pathogenesis. Though the deleterious effects of intracellular mutant SOD1 can not be excluded, our model of toxicity based on secreted mutant SOD1 is compatible with the idea that the disease is not autonomous to motor neurons[14].

Although the exact mechanisms underlying the microgliosis and neurotoxicity of extracellular mutant SOD1 remain to be elucidated, various deleterious effects of misfolded SOD1 proteins may occur through generation of hydroxyl radicals[7], toxic oligomers[11] or amyloid-like filaments[43]. This model would support a linkage between inflammation and ALS pathogenesis[44,45]. Many factors may contribute to motor neuron death in the context of inflammation. Proinflammatory molecules such as TNF-α, Fas ligand or nitric oxide may act as mediators of motor neuron death[8]. Microglial activation alone is not usually sufficient to induce motor neuron death. For instance, induction of innate immunity by intraperitoneal injection of LPS does not injure motor neurons[44]. Chronic LPS administration precipitated ALS in mice, however, supporting the view that chronic inflammation may constitute a risk factor[44]. Yet, our data demonstrate that elimination of microglia by LLME did not alter survival of motor neurons and that LPS is much less toxic to motor neurons than mutant SOD1 in mixed embryonic spinal cord cultures (**Fig. 8b,e**). It is noteworthy that mutant SOD1, and to some extent wild-type SOD1, can be converted to toxic species even in absence of copper and zinc (**Fig. 8c**). This concurs with previous reports about the misfolded nature of apo-state SOD1 (refs. 16,43).

In conclusion, our results suggest a novel function for chromogranins in mediating the secretion of misfolded SOD1 mutants, a potentially toxic pathway that can induce inflammation and neuronal death. In future studies, it will be of interest to determine whether chromogranin-mediated secretion may be applicable to other neurodegenerative diseases that involve misfolded proteins.

METHODS

Materials. Commercially available antibodies are listed in **Supplementary Methods** online. The Golgi marker plasmid DsRed-Golgi, which carries the Golgi-targeting sequence of the human gene encoding β1,4-galactosyl transferase, was a generous gift from Y. Imai (RIKEN Brain Science Institute).

To generate an antibody specific to the N′ terminus of mouse CgA, we immunized rabbits with the peptide CLPVNSPMTKGDTKVMK, which encodes the amino terminal residues of mature mouse CgA (amino acids 18–35). The antisera were purified with an affinity column coupled with the same antigen. The titer and specificity were investigated by western blotting (**Supplementary Fig. 4**).

The recombinant proteins of human SOD1 (wild-type and mutant) and mouse CgA were generated from *Escherichia coli* as described in **Supplementary Methods**.

Transgenic mice. Transgenic mice harboring the G93A mutant of human SOD1 (*B6SJL-TgN[SOD1-G93A]^(dl)1Gur*, *B6SJL-TgN[SOD1-G93A]1Gur*) and those harboring wild-type human SOD1 (*C57Bl/6-TgN[SOD1]3Cje*, *hSOD1^WT*) were purchased from The Jackson Laboratory. Transgenic mice carrying G37R *SOD1* (line 29) were a kind gift from D. Cleveland (University of California, San Diego) and were housed and bred with C57Bl/6 mice. We selected these mouse lines because they were readily available to us. Since we maintain a larger colony of G37R *SOD1* (line 29) mice, most of our experiments involving mouse analysis were done with this line. Mice were treated with 10% chloral hydrate for anesthesia before they were perfused or killed. Animals were handled in accordance with the approved protocol by the animal experiment committees at RIKEN Brain Science Institute and by the Comité de Protection des Animaux de l'Université Laval.

Yeast two-hybrid screening. The plasmid *pGilda* carrying the G93A *SOD1* mutant was generated as bait for library screening. Yeast two-hybrid analysis (LexA/transactivation system) was performed on a cDNA library (1.5 × 10^{6} independent clones) ligated into the *pJG4,5* plasmid from the total spinal cords of five preclinical transgenic mice carrying human G93A *SOD1* (*B6SJL-Tg(SOD1-G93A)1Gur/J*). Yeast two-hybrid screening was carried out using the Matchmaker Two-Hybrid System (Clontech) according to the manufacturer's protocol. There were 250 blue colonies that survived on the agar plates that contained galactose/raffinose and X-gal, but lacked tryptophan, histidine, leucine and uracil. All 250 were sequenced.

Plasmids, cell culture and transfection. Expression plasmids harboring human *SOD1* (wild-type, A4V, G85R or G93A) were prepared as reported previously[11]. The full-length murine genes encoding CgA (*Chga*) or CgB (*Chgb*) were cloned by RT-PCR using polyA-RNA from total brain of adult normal mice of the C57Bl/6 strain. See **Supplementary Methods** and **Supplementary Table 1** online for construction of EGFP-tagged CgB or deletion mutants of CgB. Cells from the murine neuroblastoma cell line Neuro2a, from the mouse fibroblast cell line NIH3T3 and COS-7 monkey ovary cells were maintained in nutrient medium containing 10% fetal bovine serum in the Dulbecco's minimal essential medium (DMEM, Sigma). The mouse microglial BV2 cells were cultured in DMEM-F12 Ham's (DF) medium containing 10% FBS. Cells were used for transfection using Lipofectamine Plus (Invitrogen) according to the manufacturer's protocol.

Immunoblotting and immunoprecipitation of cultured cells. Cells were lysed in TNT-G buffer consisting of 50 mM Tris-HCl (pH 7.4), 150 mM NaCl and 1% Triton-X100 with protease inhibitor cocktail (Roche) 24 h after the transfection. The cell lysates were incubated with anti-FLAG M2 agarose affinity gel (Sigma) for 1 h at 4 °C and were eluted with 4% SDS sample buffer. Samples were resolved by SDS-PAGE and transferred to a PVDF membrane (Polyscreen, PerkinElmer). A western blot image was obtained using a chemiluminescence detection kit (PerkinElmer).

Immunofluorescence and immunohistochemistry. Fixation of the cells and preparation of spinal cord slices is described in **Supplementary Methods**. After blocking, cultures or sections were incubated with primary antibodies and subsequently with corresponding fluorescent secondary antibodies (Alexa, Invitrogen) or with biotinylated secondary antibodies visualized by the avidin-biotin-immunoperoxidase complex (ABC) method using a Vectastain ABC kit (Vector Laboratories) and 3.3′-diaminobenzidine tetrahydrochloride (DAB; Sigma). The dilution rate of the primary antibodies is indicated in **Supplementary Methods**. Cells and tissue sections were observed by confocal laser microscopy (Olympus).

Subcellular fractionation of the spinal cord lysates. Spinal cord tissues from different ages of human *SOD1* transgenic mice were subcellularly fractionated into cytosolic, heavy and light membrane fractions, as described in **Supplementary Methods**. The protein concentration was determined by Bradford assay (BioRad), and an equal amount of protein was analyzed by western blotting. The percentage distribution of hSOD1 in post-nuclear fractions was also obtained by densitometric analysis and calculation of proportion from initial volume.

Sucrose-gradient ultracentrifugation of microsome fraction from spinal cord lysates. The light membrane (microsomal) fraction from spinal cord of G37R *SOD1* mice was further separated by sucrose gradient ultracentrifugation as previously described[46], with minor modifications that are decribed in **Supplementary Methods**. After overnight ultracentrifugation in sucrose cushions (5%, 30% and 40%), one-tenth (0.42 ml) was taken from the top of each sample, and the pellet was resuspended in MBS with 2 mM EDTA and 1% Triton-X100, and then concentrated using a centrifugal filter (Millipore) to 100 μl. Each fraction (20 μl) was separated by SDS-PAGE and analyzed by western blotting.

Immuno-isolation of TGN. To obtain pure preparations of TGN, we generated rabbit polyclonal antibody specific to the amino terminal peptides (CEGKRSKVTRRPKASDYQRLNLKL) of mouse/rat TGN38, a surface marker of TGN[47]. This anti-TGN38 or rabbit control IgG was bound to protein

G-coated magnetic beads (Dynal) and was incubated with precleared post-mitochondrial fractions (described in more detail in **Supplementary Methods**). After washing, immunoprecipitates were eluted by 4% SDS sampling buffer and analyzed by western blotting with human SOD1-specific antibody (StressGen).

Immunoprecipitation of spinal cord lysates. The post-mitochondrial fractions of spinal cords were prepared by the same protocol as those in the immuno-isolation experiments. Rabbit polyclonal antibodies to CgA or CgB (Santa Cruz) or rabbit control IgG was bound to protein G-coated magnetic beads and incubated with precleared lysates, as described in **Supplementary Methods**. Immunoprecipitates were analyzed by Western blotting with human SOD1-specific antibody (StressGen).

Immunoelectron microscopy. We used post-embedding immunohistochemistry for electron microscopic observation, in which ultra-thin sections on the nickel grids were processed for immunohistochemistry without osmication. Fixation of the mice and preparation of ultrathin sections are described in **Supplementary Methods**. After blocking, grids were incubated with primary antibodies in the same buffer at 4 °C overnight, followed by a reaction with immunogold-conjugated secondary antibody (10 nm or 5 nm) for 1 h at 22 °C. For double staining, grids were further processed using another immuno-reaction with a different primary and the secondary antibody with differently sized gold particles. Grids were observed by a TECNAI 12 electron microscope (FEI company).

Secretion assays. COS-7 and NIH3T3 cells were used in secretion experiments as non-neuronal cells lacking secretory granules[33]. At 24 h after transfection, cells plated onto a 6-well culture dish were washed in prewarmed PBS twice. Cells were incubated in basal secretion medium containing 10 mM HEPES, 129 mM NaCl, 5 mM NaHCO₃, 4.8 mM KCl, 1.2 mM MgCl₂, 1.2 mM KH₂PO₄, 1 mM CaCl₂ and 2.8 mM glucose (pH 7.4) for 1 h, and then treated with 1 ml of secretagogue-containing medium (stimulation buffer: 10 mM Hepes, 79 mM NaCl, 5 mM NaHCO₃, 50 mM KCl, 1.2 mM KH₂PO₄, 1.2 mM MgCl₂, 2 mM BaCl₂, 2.8 mM glucose, pH 7.4) for 15 min. In some experiments, Brefeldin A (BFA, 5 μM) was applied before exposure to stimulation medium. Lactacystin was applied in some assays 3 h after transfection and before incubation with basal buffer. We then collected 950 μl of medium and centrifuged it for 5 min at 1,000*g* to remove the debris. The supernatants were concentrated by a protein concentrator with 3.5 kDa cut-off (Millipore) to 60 μl, followed by western analysis. Secreted SOD1 was estimated by standardization with intracellular SOD1 in total cell lysates.

Primary cultures from embryonic spinal cord of transgenic mice carrying human *SOD1* (wild-type or *G37R*) were also investigated by secretion analysis. Cultures were prepared as explained below. Cell suspension from one spinal cord was plated onto one chamber in a six-well culture plate coated with polyethyleneimine. Secretion experiments were done after 14 d of culture *in vitro* using the protocol described above.

The content of LDH in the culture medium was measured in the medium 24 h after transfection using an LDH assay kit (Promega) according to the manufacture's protocol. Cells transfected with empty vector were used as a control.

Semi-quantitative reverse transcription PCR of microglial cell lines. Neuro2a cells were co-transfected with *pcDNA-SOD1* (wild-type, *G85R* or *G93A*) and *pcDNA3-CgA* in DF medium containing 10% FBS. At 16 h after transfection, the conditioned medium was transferred into the culture wells where BV2 cells had been previously plated, then further incubated for 24 h. Alternatively, BV2 cells were treated directly with recombinant proteins for 24 h. Then, cells were washed twice in PBS and total RNA was extracted using Trizol (Invitrogen). RT-PCR was conducted using oligo-dT primers according to the manufacturer's protocol (Invitrogen). The sequence of primer pairs is shown in **Supplementary Table 2** online. The gel images of PCR products obtained from illuminator were scanned, and densitometric analysis was performed using Scion image (Scion Corp.).

Primary culture of mouse embryonic spinal cord. Dissociated cultures of embryonic murine spinal cord were grown as previously described[11]. The spinal

ARTICLES

cultures were treated at 11 or 14 d after plating. Motor neurons were identified as large cells labeled with SMI32 and active microglia were detected with Mac2-specific antibody. Confocal microscopy images were obtained from eight randomly selected fields, and immunoreactive cells were counted by computer. In several experiments, microglia were eliminated by a 16-h treatment with LLME[36] before exposure to recombinant SOD1 proteins. In preliminary experiments, we noticed that 5-mM LLME for 16 h killed approximately 60–70% of Mac2-positive cells. The number of cells was calculated as cells per mm^2 and averaged. Statistical significance was evaluated by single-factor ANOVA (analysis of variance) following Scheffe's method.

Note: Supplementary information is available on the Nature Neuroscience website.

Published online at http://www.nature.com/natureneuroscience/
Reprints and permissions information is available online at http://npg.nature.com/reprintsandpermissions/

1. Rosen, D.R. *et al.* Mutations in Cu/Zn superoxide dismutase gene are associated with familial amyotrophic lateral sclerosis. *Nature* **362**, 59–62 (1993).
2. Gurney, M.E. *et al.* Motor neuron degeneration in mice that express a human Cu,Zn superoxide dismutase mutation. *Science* **264**, 1772–1775 (1994).
3. Subramaniam, J.R. *et al.* Mutant SOD1 causes motor neuron disease independent of copper chaperone-mediated copper loading. *Nat. Neurosci.* **5**, 301–307 (2002).
4. Wang, J., Xu, G. & Borchelt, D.R. High molecular weight complexes of mutant superoxide dismutase 1: age-dependent and tissue-specific accumulation. *Neurobiol. Dis.* **9**, 139–148 (2002).
5. Julien, J.P. Amyotrophic lateral sclerosis. unfolding the toxicity of the misfolded. *Cell* **104**, 581–591 (2001).
6. Cleveland, D.W. & Rothstein, J.D. From Charcot to Lou Gehrig: deciphering selective motor neuron death in ALS. *Nat. Rev. Neurosci.* **2**, 806–819 (2001).
7. Wiedau-Pazos, M. *et al.* Altered reactivity of superoxide dismutase in familial amyotrophic lateral sclerosis. *Science* **271**, 515–518 (1996).
8. Raoul, C. *et al.* Motoneuron death triggered by a specific pathway downstream of Fas: potentiation by ALS-linked SOD1 mutations. *Neuron* **35**, 1067–1083 (2002).
9. Durham, H.D., Roy, J., Dong, L. & Figlewicz, D.A. Aggregation of mutant Cu/Zn superoxide dismutase proteins in a culture model of ALS. *J. Neuropathol. Exp. Neurol.* **56**, 523–530 (1997).
10. Johnston, J.A., Dalton, M.J., Gurney, M.E. & Kopito, R.R. Formation of high molecular weight complexes of mutant Cu, Zn-superoxide dismutase in a mouse model for familial amyotrophic lateral sclerosis. *Proc. Natl. Acad. Sci. USA* **97**, 12571–12576 (2000).
11. Urushitani, M., Kurisu, J., Tsukita, K. & Takahashi, R. Proteasomal inhibition by misfolded mutant superoxide dismutase 1 induces selective motor neuron death in familial amyotrophic lateral sclerosis. *J. Neurochem.* **83**, 1030–1042 (2002).
12. Pramatarova, A., Laganière, J., Roussel, J., Brisebois, K. & Rouleau, G.A. Neuron-specific expression of mutant superoxide dismutase 1 in transgenic mice does not lead to motor impairment. *J. Neurosci.* **21**, 3369–3374 (2001).
13. Lino, M.M., Schneider, C. & Caroni, P. Accumulation of SOD1 mutants in postnatal motoneurons does not cause motoneuron pathology or motoneuron disease. *J. Neurosci.* **22**, 4825–4832 (2002).
14. Clement, A.M. *et al.* Wild-type nonneuronal cells extend survival of SOD1 mutant motor neurons in ALS mice. *Science* **302**, 113–117 (2003).
15. Shinder, G.A., Lacourse, M.C., Minotti, S. & Durham, H.D. Mutant Cu/Zn-superoxide dismutase proteins have altered solubility and interact with heat shock/stress proteins in models of amyotrophic lateral sclerosis. *J. Biol. Chem.* **276**, 12791–12796 (2001).
16. Urushitani, M. *et al.* CHIP promotes proteasomal degradation of familial ALS-linked mutant SOD1 by ubiquitinating Hsp/Hsc70. *J. Neurochem.* **90**, 231–244 (2004).
17. Taupenot, L., Harper, K.L. & O'Connor, D.T. The chromogranin-secretogranin family. *N. Engl. J. Med.* **348**, 1134–1149 (2003).
18. Rudolf, R., Salm, T., Rustom, A. & Gerdes, H.H. Dynamics of immature secretory granules: role of cytoskeletal elements during transport, cortical restriction, and f-actin-dependent tethering. *Mol. Biol. Cell* **12**, 1353–1365 (2001).

19. Li, J.Y., Leitner, B., Lovisetti-Scamihorn, P., Winkler, H. & Dahlström, A. Proteolytic processing, axonal transport and differential distribution of chromogranins A and B, and secretogranin II (secretoneurin) in rat sciatic nerve and spinal cord. *Eur. J. Neurosci.* **11**, 528–544 (1999).
20. Booj, S., Goldstein, M., Fischer-Colbrie, R. & Dahlstrom, A. Calcitonin gene-related peptide and chromogranin A: presence and intra-axonal transport in lumbar motor neurons in the rat, a comparison with synaptic vesicle antigens in immunohistochemical studies. *Neuroscience* **30**, 479–501 (1989).
21. Marksteiner, J. *et al.* Distribution of chromogranin B-like immunoreactivity in the human hippocampus and its changes in Alzheimer's disease. *Acta Neuropathol. (Berl.)* **100**, 205–212 (2000).
22. Rangon, C.M. *et al.* Different chromogranin immunoreactivity between prion and a-beta amyloid plaque. *Neuroreport* **14**, 755–758 (2003).
23. Schiffer, D., Cordera, S., Giordana, M.T., Attanasio, A. & Pezzulo, T. Synaptic vesicle proteins, synaptophysin and chromogranin A in amyotrophic lateral sclerosis. *J. Neurol. Sci.* **129** Suppl, 68–74 (1995).
24. Taupenot, L. *et al.* Chromogranin A triggers a phenotypic transformation and the generation of nitric oxide in brain microglial cells. *Neuroscience* **72**, 377–389 (1996).
25. Ciesielski-Treska, J. *et al.* Mechanisms underlying neuronal death induced by chromogranin A-activated microglia. *J. Biol. Chem.* **276**, 13113–13120 (2001).
26. Taylor, D.L., Diemel, L.T. & Pocock, J.M. Activation of microglial group III metabotropic glutamate receptors protects neurons against microglial neurotoxicity. *J. Neurosci.* **23**, 2150–2160 (2003).
27. Chanat, E., Weiss, U., Huttner, W.B. & Tooze, S.A. Reduction of the disulfide bond of chromogranin B (secretogranin I) in the trans-Golgi network causes its missorting to the constitutive secretory pathways. *EMBO J.* **12**, 2159–2168 (1993).
28. Cowley, D.J., Moore, Y.R., Darling, D.S., Joyce, P.B. & Gorr, S.U. N- and C-terminal domains direct cell type-specific sorting of chromogranin A to secretory granules. *J. Biol. Chem.* **275**, 7743–7748 (2000).
29. Li, J.Y., Kling-Petersen, A. & Dahlstrom, A. Influence of spinal cord transection on the presence and axonal transport of CGRP-, chromogranin A-, VIP-, synapsin I-, and synaptophysin-like immunoreactivities in rat motor nerve. *J. Neurobiol.* **23**, 1094–1110 (1992).
30. Kato, A. *et al.* Co-distribution patterns of chromogranin B-like immunoreactivity with chromogranin A and secretoneurin within the human brainstem. *Brain Res.* **852**, 444–452 (2000).
31. Stieber, A. *et al.* Disruption of the structure of the Golgi apparatus and the function of the secretory pathway by mutants G93A and G85R of Cu, Zn superoxide dismutase (SOD1) of familial amyotrophic lateral sclerosis. *J. Neurol. Sci.* **219**, 45–53 (2004).
32. Ciesielski-Treska, J. *et al.* Chromogranin A induces a neurotoxic phenotype in brain microglial cells. *J. Biol. Chem.* **273**, 14339–14346 (1998).
33. Huh, Y.H., Jeon, S.H. & Yoo, S.H. Chromogranin B-induced secretory granule biogenesis: comparison with the similar role of chromogranin A. *J. Biol. Chem.* **278**, 40581–40589 (2003).
34. Turner, B.J. *et al.* Impaired extracellular secretion of mutant superoxide dismutase 1 associates with neurotoxicity in familial amyotrophic lateral sclerosis. *J. Neurosci.* **25**, 108–117 (2005).
35. Jacobsson, J., Jonsson, P.A., Andersen, P.M., Forsgren, L. & Marklund, S.L. Superoxide dismutase in CSF from amyotrophic lateral sclerosis patients with and without CuZn-superoxide dismutase mutations. *Brain* **124**, 1461–1466 (2001).
36. Sharpless, N. *et al.* The restricted nature of HIV-1 tropism for cultured neural cells. *Virology* **191**, 813–825 (1992).
37. Miyakawa, K. & Imamura, T. Secretion of FGF-16 requires an uncleaved bipartite signal sequence. *J. Biol. Chem.* **278**, 35718–35724 (2003).
38. Tiwari, A. & Hayward, L.J. Familial amyotrophic lateral sclerosis mutants of copper/zinc superoxide dismutase are susceptible to disulfide reduction. *J. Biol. Chem.* **278**, 5984–5992 (2003).
39. Tobisawa, S. *et al.* Mutant SOD1 linked to familial amyotrophic lateral sclerosis, but not wild-type SOD1, induces ER stress in COS7 cells and transgenic mice. *Biochem. Biophys. Res. Commun.* **303**, 496–503 (2003).
40. Lafon-Cazal, M. *et al.* Proteomic analysis of astrocytic secretion in the mouse. Comparison with the cerebrospinal fluid proteome. *J. Biol. Chem.* **278**, 24438–24448 (2003).
41. Cimini, V. *et al.* CuZn-superoxide dismutase in human thymus: immunocytochemical localisation and secretion in thymus-derived epithelial and fibroblast cell lines. *Histochem. Cell Biol.* **118**, 163–169 (2002).
42. Nickel, W. The mystery of nonclassical protein secretion. A current view on cargo proteins and potential export routes. *Eur. J. Biochem.* **270**, 2109–2119 (2003).
43. Elam, J.S. *et al.* Amyloid-like filaments and water-filled nanotubes formed by SOD1 mutant proteins linked to familial ALS. *Nat. Struct. Biol.* **10**, 461–467 (2003).
44. Nguyen, M.D., D'Aigle, T., Gowing, G., Julien, J.P. & Rivest, S. Exacerbation of motor neuron disease by chronic stimulation of innate immunity in a mouse model of amyotrophic lateral sclerosis. *J. Neurosci.* **24**, 1340–1349 (2004).
45. Zhu, S. *et al.* Minocycline inhibits cytochrome c release and delays progression of amyotrophic lateral sclerosis in mice. *Nature* **417**, 74–78 (2002).
46. Parkin, E.T., Hussain, I., Karran, E.H., Turner, A.J. & Hooper, N.M. Characterization of detergent-insoluble complexes containing the familial Alzheimer's disease-associated presenilins. *J. Neurochem.* **72**, 1534–1543 (1999).
47. Stephens, D.J. & Banting, G. Direct interaction of the trans-Golgi network membrane protein, TGN38, with the F-actin binding protein, neurabin. *J. Biol. Chem.* **274**, 30080–30086 (1999).

Unsaturated Fatty Acids Induce Cytotoxic Aggregate Formation of Amyotrophic Lateral Sclerosis-linked Superoxide Dismutase 1 Mutants*

Yeon-Jeong Kim‡, Reiko Nakatomi§, Takumi Akagi§, Tsutomu Hashikawa§, and Ryosuke Takahashi‡¶‖

From the Laboratories for ‡Motor System Neurodegeneration and §Neural Architecture, RIKEN Brain Science Institute, Saitama 351-0198, Japan and ¶Department of Neurology, Kyoto University Graduate School of Medicine, Kyoto 606-8507, Japan

Formation of misfolded protein aggregates is a remarkable hallmark of various neurodegenerative diseases including Alzheimer disease, Parkinson disease, Huntington disease, prion encephalopathies, and amyotrophic lateral sclerosis (ALS). Superoxide dismutase 1 (SOD1) immunoreactive inclusions have been found in the spinal cord of ALS animal models and patients, implicating the close involvement of SOD1 aggregates in ALS pathogenesis. Here we examined the molecular mechanism of aggregate formation of ALS-related SOD1 mutants *in vitro*. We found that long-chain unsaturated fatty acids (FAs) promoted aggregate formation of SOD1 mutants in both dose- and time-dependent manners. Metal-deficient SOD1s, wild-type, and mutants were highly oligomerized compared with holo-SOD1s by incubation in the presence of unsaturated FAs. Oligomerization of SOD1 is closely associated with its structural instability. Heat-treated holo-SOD1 mutants were readily oligomerized by the addition of unsaturated FAs, whereas wild-type SOD1 was not. The monounsaturated FA, oleic acid, directly bound to SOD1 and was characterized by a solid-phase FA binding assay using oleate-Sepharose. The FA binding characteristics were closely correlated with the oligomerization propensity of SOD1 proteins, which indicates that FA binding may change SOD1 conformation in a way that favors the formation of aggregates. High molecular mass aggregates of SOD1 induced by FAs have a granular morphology and show significant cytotoxicity. These findings suggest that SOD1 mutants gain FA binding abilities based on their structural instability and form cytotoxic granular aggregates.

Amyotrophic lateral sclerosis (ALS)[1] is a progressive and fatal neurodegenerative disorder that mainly affects motor neurons in the brain stem and spinal cord. Approximately 10% of ALS patients are familial cases, with autosomal dominant inheritance. More than 90 different mutations in the gene coding for superoxide dismutase 1 (SOD1) have been identified in about 20% of familial ALS (FALS) families (1, 2). Although the molecular mechanisms of selective motor neuron degeneration by SOD1 mutants in FALS remain largely unknown, common pathological features of conformational diseases, as evidenced by SOD1 immunoreactive inclusions, are found in the spinal cord of ALS patients and in the SOD1 mutant FALS mouse model (3–8). The characteristics of FALS resemble those of many other neurodegenerative diseases in which a causative protein undergoes a conformational rearrangement, which endows it with a tendency to aggregate and form deposits within affected tissues.

SOD1 is a 32-kDa homodimeric enzyme that decreases the intracellular concentration of superoxide radicals by catalyzing their dismutation to O_2 and H_2O_2. ALS-linked mutations of SOD1 are distributed throughout the primary and tertiary structures, and most mutations appear unrelated to the dismutase activity. Many biochemical and biophysical studies have reported that SOD1 mutants are structurally unstable compared with wild-type forms (10–13). These observations suggest that the mutations primarily affect the structural stability of SOD1 rather than the enzyme activity.

The half-life of SOD1 mutants is shorter than that of wild-type forms in cultured cells (14). SOD1 mutants form a complex with Hsp70 and CHIP, which promotes degradation of SOD1 through the ubiquitin-proteasome system (15). Hsp70 directly binds metal-deficient wild-type SOD1 as well as SOD1 mutants, suggesting that destabilized SOD1 is targeted by the molecular chaperone system (15, 16). These observations imply that structural stability of SOD1 may also be strongly involved in refolding by the chaperone or in degradation of SOD1 by the ubiquitin-proteasome system. On the other hand, aggregates of mutant SOD1 are observed to have aggresome-like morphology when cells are treated with a proteasome inhibitor (14). This aggresome-like morphology resembles pathological inclusions of neurodegenerative diseases in affected tissues. These findings suggest that in disease states, misfolded proteins overwhelm the protein handling systems, including chaperones and proteasomes. Therefore, the formation of cellular inclusions may be required for other factors to act as modulators to promote protein aggregates. In fact, lipid molecules, including unsaturated fatty acids (FAs), phosphatidylserine, and phosphatidylinositol, promote amyloidogenesis of amyloid β-peptides, tau (17), and α-synuclein (18, 19) *in vitro*. These molecules are biologically significant as mediators for signal-

---

‖ To whom correspondence should be addressed: Dept. of Neurology, Kyoto University Graduate School of Medicine, 54 Kawahara-cho, Shogoin, Sakyo-ku, Kyoto 606-8507, Japan. Tel.: 81-75-751-3770; Fax: 81-75-761-9780; E-mail: ryosuket@kuhp.kyoto-u.ac.jp.

[1] The abbreviations used are: ALS, amyotrophic lateral sclerosis; FALS, familial amyotrophic lateral sclerosis; SOD1, superoxide dismutase 1; FA, fatty acid; AA, arachidonic acid; MTS, 3-(4,5-dimethylthiazol-2-yl)-5-(3-carboxymethoxyphenyl)-2-(4-sulfophenyl)-2H-tetrazolium.

ing and inflammation during disease progression of neurodegeneration.

Here we investigated *in vitro* SOD1 aggregation affected by FAs to create an aggregation model system for FALS. We demonstrated that unsaturated FAs promote self-assembly and cytotoxic aggregate formation of SOD1. Aggregation by FAs is strongly correlated with structural instability and FA binding activity of SOD1, which may have significant implications in FALS.

EXPERIMENTAL PROCEDURES

Expression, Purification, and Characterization of Recombinant SOD1 Proteins—pcDNA3-SOD1 (20) was digested with EcoRV and XhoI and subcloned into blunted NcoI and XhoI sites of pET-15(b) (Novagen) to construct the expression plasmid. Expression of recombinant SOD1 proteins was induced in BL21(DE3)pLysS by adding 1 mM isopropyl 1-thio-β-D-galactopyranoside, 0.1 mM $CuCl_2$, and 0.1 mM $ZnCl_2$ until cells were grown to 0.6 absorbance unit at 600 nm, and then bacterial cells were further cultured at 23 °C for 6 h. Cells were pelleted and resuspended in TNE buffer (50 mM Tris-HCl, pH 8.0, 150 mM NaCl, and 0.1 mM EDTA) supplemented with protease inhibitor mixture (Roche Applied Science). Cells were then disrupted by sonication. Insoluble materials were removed by centrifugation at 10,000 $\times$ g for 30 min. Supernatant was collected for further purification. Purification was performed according to Hayward *et al.* (11), with minor modifications. Briefly, ammonium sulfate powder was added to the supernatant to 65% saturation with gentle stirring on ice. The supernatant, after centrifugation at 10,000 $\times$ g for 30 min, was directly loaded for phenyl-Sepharose (Amersham Biosciences) column chromatography. The column was thoroughly washed with TNE buffer containing 2 M ammonium sulfate. Proteins were eluted using a linearly decreasing salt gradient. SOD1 activity measurement using a xanthine/xanthine oxidase-based method (21) identified fractions containing SOD1. Activity fractions were desalted by ultrafiltration using a centricon filter (Millipore). SOD1 was re-metallated as described previously (22). The proteins were then loaded onto a Q-Sepharose (Amersham Biosciences) anion exchange column and eluted using a linearly increasing salt gradient toward a buffer containing 200 mM NaCl and 10 mM Tris-HCl, pH 8.0. Fractions containing SOD1 were pooled and concentrated. Homogeneity of SOD1 was >95%, as verified by SDS-PAGE with Coomassie Brilliant Blue staining. Specific activity of the purified enzymes was assayed and calculated by bovine SOD1 (Cayman) or human SOD1 purified from erythrocytes (Sigma-Aldrich) as standards. Fully metallated SOD1 was delipidated using hydroxyalkoxypropyl dextran type III (Sigma-Aldrich) as described previously (19) before de-metallation. Metal-deficient apo-enzymes were prepared as described previously (23), and loss of enzyme activity was confirmed after de-metallation. The metal content of purified enzymes was estimated as described previously (22).

Oligomerization of SOD1—A stock solution of 25 mM FAs was prepared in 0.01 M NaOH containing 25 μM butylated hydroxytoluene. SOD1 proteins were filtered through Microcon YM-100 (100-kDa cutoff) filters (Millipore) to remove high molecular mass SOD1 before oligomerization. FAs were added directly to preincubated SOD1 at 37 °C in 50 mM phosphate buffer, pH 7.2, containing 150 mM NaCl and 0.1 mM EDTA and further incubated at the same temperature.

SDS-PAGE and Western Blotting—For detection of SOD1 oligomers, SDS-PAGE was performed under non-reducing conditions using 12.5% polyacrylamide gels. After oligomerization of SOD1, protein samples were prepared in SDS-PAGE loading buffer (62.5 mM Tris-HCl, pH 6.8, 1% SDS, 5% glycerol, and 0.007% bromphenol blue) in the absence of β-mercaptoethanol and then boiled at 95 °C for 3 min before loading. Western blotting was performed as described previously (24). Briefly, proteins were transferred to Hybond ECL nitrocellulose membranes (Amersham Biosciences), followed by UV cross-linking, boiling membranes in 2% SDS and 50 mM Tris, pH 7.6, for 10 min, and extensive washing in Tris-buffered saline. For detection of SOD1, rabbit anti-SOD1 antibody (Stressgen) was used.

Glycerol Density Gradient Centrifugation and Densitometric Analysis—A glycerol linear gradient of 10–40% was prepared in a centrifuge tube. Formation of the SOD1 oligomer was performed as described above. Approximately 200 μl of incubated SOD1 was layered onto a glycerol cushion and separated by centrifugation with a SW41Ti rotor (Beckman) at 35,000 rpm for 15 h. In a parallel experiment, protein standards (Amersham Biosciences) were separated simultaneously in order to calibrate fractions. Fractions were subjected to SDS-PAGE

under non-reducing conditions, and then Western blotting was performed. Western blot images were analyzed using image analysis software (Scion Image Beta 4.02; Scion Corp.).

Solid-phase Oleic Acid Binding—Sodium salt of oleic acid (Sigma-Aldrich) was coupled to EAH-Sepharose (Amersham Biosciences) by 1-ethyl-3-(3-dimethylaminopropyl)-carbodiimide (Pierce) to prepare oleate-Sepharose according to Peters *et al.* (25). Oleic acid coupling was verified by binding bovine serum albumin and recombinant α-synuclein protein. Mock-Sepharose was prepared from EAH-Sepharose by blocking coupling ligand with 1 M acetic acid. For the binding assay, 200 ng of Microcon-filtered protein was incubated with oleate-Sepharose or mock-Sepharose in 400 μl of phosphate-buffered saline containing 0.1 mM EDTA at 37 °C for 30 min with agitation. Protein bound to Sepharose was settled on a spun column and washed extensively with phosphate-buffered saline. The bound protein was then eluted with 50% ethanol. Eluates were subjected to SDS-PAGE and Western blotting.

Transmission Electron Microscopy—SOD1 proteins (40 μM) were incubated at 37 °C for 24 h in 50 mM phosphate buffer (pH 7.2) containing 150 mM NaCl and 0.1 mM EDTA supplemented with 100 μM arachidonic acid. The samples were absorbed to a glow-charged supporting membrane on 400-mesh grids and fixed by floating on 2.5% glutaraldehyde and 4% paraformaldehyde in 0.1 M phosphate buffer for 5 min. After three washes with distilled water, samples were negatively stained by 2% sodium phosphotungstic acid and dried. Specimens were observed in a LEO 912AB electron microscope (LEO Electron Microscopy), operated at 100 kV.

Toxicity Assay—Cytotoxicity of protein aggregates was measured as described previously (26, 27). In brief, neuro2a mouse neuroblastoma cells were maintained in Dulbecco's modified Eagle's medium with 10% fetal bovine serum and 2 mM glutamine in 5% CO_2 at 37 °C. Cells were differentiated in serum-free Dulbecco's modified Eagle's medium with 0.3 mM dibutylyl cAMP before use. Cells were plated at 30,000 cells/well in 96-well plates and differentiated overnight. The medium was removed, and prepared SOD1 aggregates were added in new medium without phenol red. After incubation for 18 h at 37 °C, the cells were assayed using an MTS reduction assay kit (Promega). Another plate also treated as described above was stained for 1 min with trypan blue, and stained cells were counted as dead cells.

RESULTS

Unsaturated Fatty Acids Promote Self-assembly of SOD1s—We expressed and homogeneously purified recombinant human SOD1s from the bacterial expression system (Fig. 1A). The purified wild-type and G93A enzymes showed comparable specific activity; however, A4V mutant showed ~56% activity compared with that of wild-type enzyme (Fig. 1B). The zinc ion content of the purified enzymes showed almost full occupancy; however, copper ion content of A4V was 54.5% of the wild-type level (Fig. 1C). Specific activity was correlated with copper ion occupancy of purified enzyme, indicating proper metal loading in the active site.

We next examined the effect of long-chain FAs on oligomerization of SOD1 proteins. Wild-type and mutant (A4V and G93A) SOD1 were incubated with various concentrations of arachidonic acid (AA) as described under "Experimental Procedures." After incubation, oligomerized SOD1 was subjected to SDS-PAGE and then detected by Western blotting. Under reducing conditions, mainly bands of ~16 and 38 kDa, corresponding to monomer and dimmer sizes of SOD1, respectively, were detected (Fig. 2A). In contrast, under non-reducing conditions, smeared patterns of >50 kDa in size were supposed to be SOD1 oligomers (Fig. 2A). These observations suggest that disulfide bonds maintained SOD1 oligomers. Thus, non-reducing SDS-PAGE was thought to be an efficient method to detect SOD1 oligomers and aggregates. Among the holo-enzymes, wild-type and G93A were not oligomerized; instead, they segregated as monomer and dimer size bands (Fig. 2B, *top panel*). After incubation with >100 μM AA, holo-A4V showed a faint smear pattern that was seen from 50 kDa to near the stacking gel range beside monomer- and dimer-size bands (Fig. 2B, *top panel*). In contrast, all metal-deficient enzymes, regardless of mutations, were oligomerized in the presence of >30 μM AA
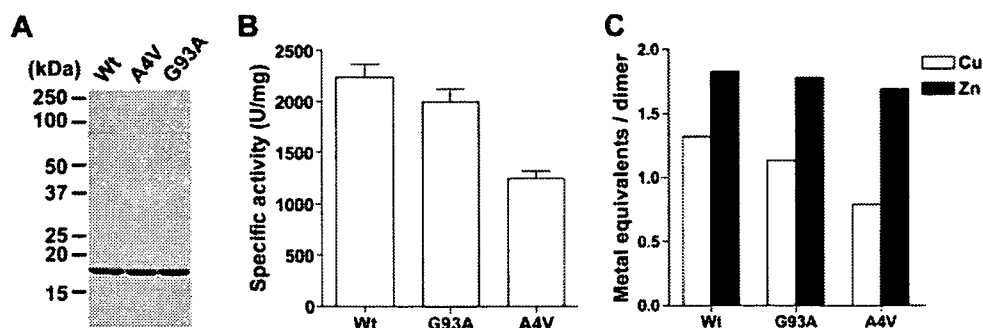
FIG. 1. **Characterization of purified recombinant SOD1s.** *A*, purified SOD1s were separated using SDS-PAGE and stained with Coomassie Brilliant Blue. *B*, dismutase activity of the purified SOD1s was assayed by the xanthine/xanthine oxidase-based method. One unit of the activity is defined as the amount of enzyme needed to exhibit 50% of dismutation of the superoxide radicals. *C*, metal content of the purified SOD1s was measured using 4-pyridylazoresorcinol assay in 6 M guanidine-HCl.
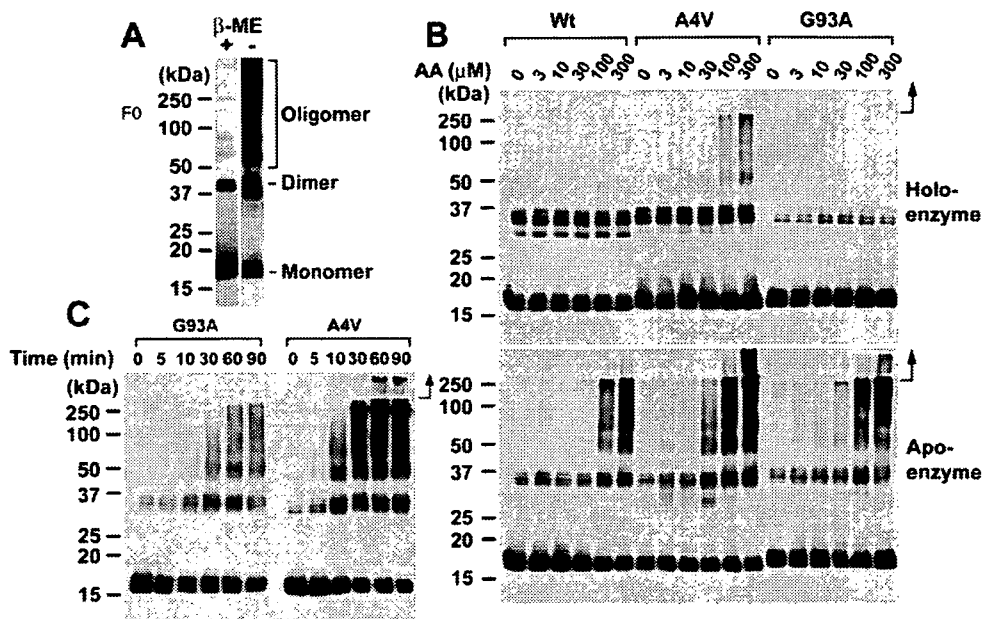

FIG. 2. **Arachidonic acid promotes SOD1 oligomerization.** *A*, FA-inducing oligomers of SOD1 were separated using SDS-PAGE with or without β-mercaptoethanol. *B*, apo-enzymes of SOD1 mutants (2.5 μM) were incubated at 37 °C in the presence of 100 μM AA. At each time point, aliquots were placed on ice to stop the reaction. *C*, purified holo- or apo-SOD1 proteins (2.5 μM) were incubated at 37 °C for 90 min in the presence of the indicated AA concentration. Incubated proteins were mixed directly with SDS-PAGE treatment buffer without reducing agents and boiled. SDS-PAGE was performed under non-reducing conditions. Proteins were detected by Western blotting as described under "Experimental Procedures." *Arrows* indicate the position of stacking gels.

(Fig. 2*B*, *bottom panel*). Apo-enzymes demonstrated higher oligomerization propensity than holo-enzymes depending on AA concentration (Fig. 2*B*). Thus, AA efficiently promoted oligomerization of SOD1s.

Next, we performed a time-course analysis of SOD1 oligomerization in the presence of AA. Metal-deficient G93A and A4V were oligomerized in a time-dependent manner (Fig. 2*C*). Maximum oligomerization was reached within 60 min of incubation in the presence of AA (Fig. 2*C*).

We then examined the effect that various FAs, including stearic acid, oleic acid, linoleic acid, and AA, have on SOD1 oligomerization. Unsaturated FAs, including oleic acid, linoleic acid, and AA, promoted SOD1 oligomerization (Fig. 3). However, saturated FAs and stearic acid had little effect on SOD1 oligomerization (Fig. 3). SOD1 oligomerization induced by FAs required at least monounsaturated FAs. This result may reflect the difference of solubility between unsaturated and saturated FAs in the buffer.

We verified the formation of SOD1 oligomers using a 10–40% glycerol density gradient centrifugation because presumable artifacts after detection of SOD1 oligomers using non-reducing SDS-PAGE may have remained. After fractionation, we could not observe high molecular mass SOD1 oligomers
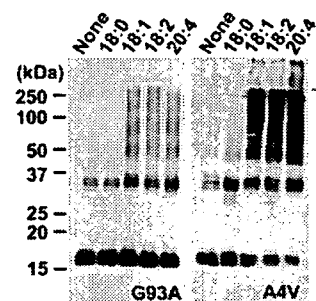
FIG. 3. **Unsaturated fatty acids affect oligomerization of SOD1.** Apo-enzymes of SOD1 mutants were incubated at 37 °C for 90 min in the presence of FAs at concentrations of 100 μM: 18:0, stearic acid; 18:1, oleic acid; 18:2, linoleic acid; and 20:4, arachidonic acid. *Arrows* indicate the position of stacking gels.

from the incubated sample in the absence of AA; fractions were <67 kDa and potentially represented monomer and dimer states (Fig. 4*A*, *top panel*). In contrast, we detected high molecular mass oligomers in fractions of >440 kDa from the incubated sample in the presence of AA (Fig. 4*A*, *bottom panel*). Under these conditions, SOD1 with molecular mass of <67 kDa was dramatically decreased compared with the sample incu-

A

B
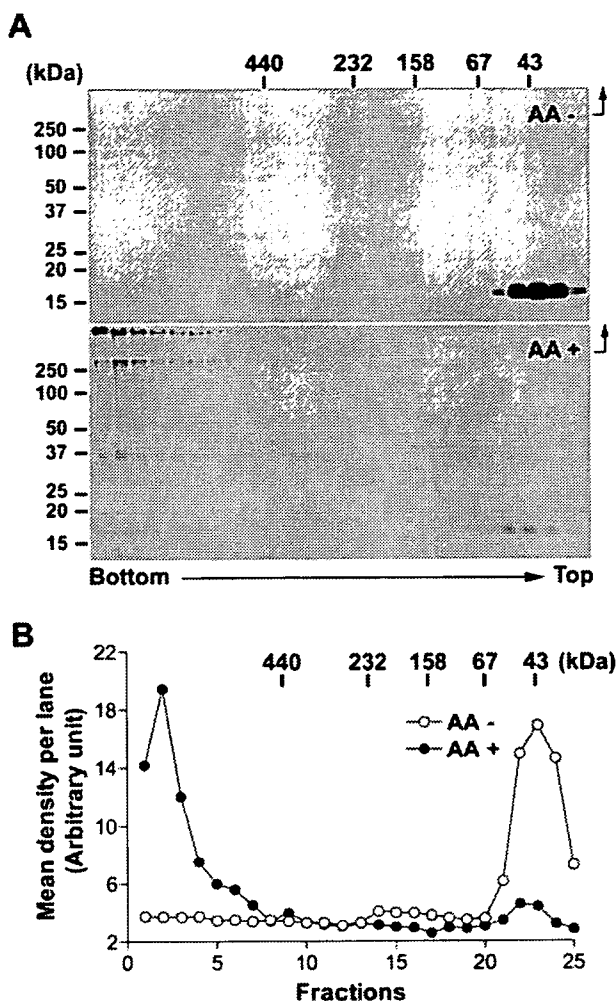
FIG. 4. **Glycerol density gradient centrifugation and densitometric analysis of SOD1 oligomers.** *A*, apo-A4V (2.5 μM) was incubated at 37 °C for 90 min in the absence or presence of 100 μM AA before loading on the glycerol cushion. After centrifugation, fractions were collected from the bottom of the tubes and then subjected to SDS-PAGE under non-reducing conditions. SOD1 proteins were detected by Western blotting. *B*, for densitometric analysis, we measured mean density per lane after background subtraction. Total mean density was similar under each condition, by calculating the mean density of visible lanes (*lanes 1–8* for oligomers and *lanes 21–25* for dimer or monomer). *Arrows* indicate the position of stacking gels.

bated in the absence of AA (Fig. 4*A*, *bottom panel*). Although oligomers of >440 kDa were fractionated by the glycerol density gradient centrifugation, these were detected as monomer, dimer, and smeared high molecular mass bands that reached stacking gels under non-reducing SDS-PAGE (Fig. 4*A*, *bottom panel*). This indicates oligomers are partly disrupted during the boiling of the SDS-PAGE loading buffer. We next performed densitometric analysis from Western blotting images to estimate the amount of oligomerized SOD1 (Fig. 4*B*). The resulting image analysis found that immunoreactivity for oligomers was ~80% of the total immunoreactivity.

Structural Instability of SOD1 Is Correlated to Oligomerization Propensity and FA Binding—We showed the FA-induced oligomerization propensity of apo-SOD1s was higher than that of holo-SOD1. This implies that protein stability might be strongly associated with FA-induced oligomerization propensity. Among the holo-enzymes, wild-type and G93A were not oligomerized under our experimental conditions (Fig. 2*B*, *top panel*). To examine the correlation between oligomerization propensity and protein stability of holo-enzymes, holo-SOD1 was heated and then oligomerized by AA. In the absence of AA,
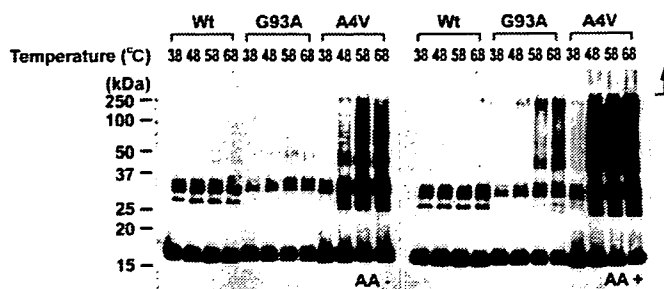
FIG. 5. **Thermally destabilized SOD1 mutants show a high oligomerization propensity.** Holo-enzymes were heat-treated at the indicated temperatures for 30 min before addition of 100 μM AA and then further incubated at 37 °C for 1 h. SDS-PAGE was performed under non-reducing conditions. Proteins were detected by Western blotting as described under "Experimental Procedures." *Arrows* indicate the position of stacking gels.

only heat-treated A4V was oligomerized (Fig. 5, *left panel*). In the presence of AA, heat-treated G93A and A4V were highly aggregated, but under the same conditions, wild-type SOD1 was not (Fig. 5, *right panel*). Oligomerization was observed above 58 °C for G93A and above 48 °C for A4V (Fig. 5, *right panel*). In the previous study, A4V was more unstable than G93A for heat treatment analyzed by differential scanning calorimetry (12). This result suggests that structural instability is strongly correlated with oligomerization propensity induced by FAs.

Although we showed that FAs promoted SOD1 oligomerization, the mechanism is not perfectly understood. Similarly, unsaturated FAs oligomerize α-synuclein and tau. In the case of α-synuclein and tau, FAs were bound to proteins, which suggested that oligomerization mechanisms underlie the FA binding characteristics of protein. To examine whether SOD1 binds to FAs, we carried out a solid-phase oleic acid binding assay. Among the holo-enzymes, very small amounts of holo-A4V were bound to the oleate-Sepharose column, whereas wild-type and G93A were not (Fig. 6*A*). All of the apo-enzymes were bound to oleate-Sepharose, regardless of their mutations (Fig. 6*A*). In contrast, bound proteins were not observed in mock-Sepharose (Fig. 6*A*). Nearly all of the input amounts of metal-deficient proteins were bound, which was estimated by 50% input. This finding suggests that metal-deficient SOD1 proteins strongly bind to FAs. We next examined whether heat-treated holo-enzymes bind to FAs. Apo-enzymes were used as control binding. Heat-treated SOD1 mutant (G93A) at 58 °C and 68 °C was bound to FAs, whereas wild-type was not (Fig. 6*B*). The results of the FA binding assay were strongly correlated with the oligomerization propensity of SOD1. These findings suggest that FA binding alters the conformation of SOD1 to form oligomers.

FA-induced SOD1 Aggregates Result in Granular Morphology and Are Cytotoxic—We analyzed the ultrastructure of SOD1 aggregates by electron microscope. SOD1 proteins (~40 μM) were incubated in the presence of 100 μM AA at 37 °C for 24 h. Holo-enzymes were heated at 50 °C for 30 min before incubation in the presence of AA. After incubation, granular aggregates were observed in all of apo-enzymes and heat-treated SOD1 mutants (Fig. 7*A*). In contrast, no visible materials were found in wild-type holo-SOD1s, even though they were heat-treated (Fig. 7*A*). The morphology of the aggregates was round or amorphous large granules composed of clustered small granules (Fig. 7*A*). We could not observe any visible protein aggregates in the samples incubated without AA, except in apo-A4V, which revealed a fibril structure (data not shown).

We next examined the effect of FA-induced aggregates on cell

viability of differentiated neuro2a cells. Aggregates of SOD1s were formed using the same methods as described for observation under an electron microscope. Aliquots incubated in the presence or absence of AA were diluted in the culture medium,
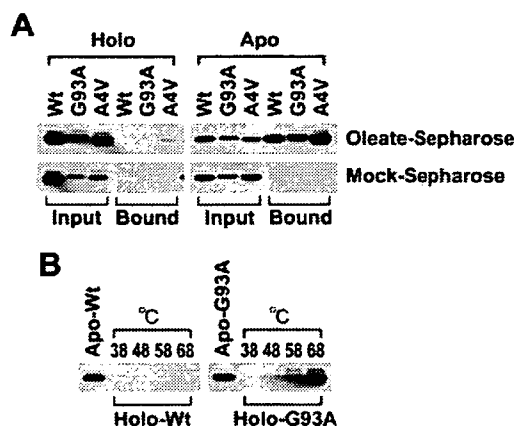
A

B

FIG. 6. **Solid-phase oleic acid binding assay shows apo-SOD1 or thermally destabilized SOD1 bound to oleate-Sepharose.** *A*, solid-phase binding assay was performed as described under "Experimental Procedures." Approximately 50% input (100 ng of proteins) was electrophoresed to estimate the quantity of FA binding SOD1. *B*, holo-SOD1s (wild-type and G93A) were thermally destabilized at the indicated temperatures for 30 min and then directly loaded on oleate-Sepharose. Apo-enzymes were used as positive controls for oleic acid binding.

which was directly added to differentiated neuro2a cells. After incubation for 18 h, toxicity was assessed with MTS reduction (Fig. 7B) and trypan blue staining (Fig. 7C). The presence of the granular aggregates formed by AA from Apo-SOD1s and heat-treated SOD1 mutants significantly reduced cell viability (Fig. 7, *B* and *C*). In contrast, no significant decrease of viability was detected when the cells were exposed either to incubated proteins in the absence of AA or to the buffer solutions used to form the aggregates in the absence of added protein (Fig. 7, *B* and *C*). These findings suggest that FA-induced SOD1 aggregates were highly toxic to the cells.

DISCUSSION

Numerous neurodegenerative diseases are accompanied by highly insoluble inclusions of protein aggregates within characteristic neuronal populations. In the case of FALS, the prototypical Lewy body-like hyaline inclusions, composed largely of granule-coated fibrils of SOD1-insoluble filaments, have been detected in the spinal cord of FALS patients with SOD1 gene mutations (5, 28). Although there has been controversy about whether such inclusions are a cause or a consequence of the neuronal degeneration, accumulating evidence suggests that aggregates formed via misfolded proteins, especially soluble oligomeric assemblies, may cause cell injury (29–31). Moreover, cytotoxicity of protein aggregates may have common features because granular aggregates form non-pathological proteins that can also be toxic (26). These findings suggest the avoidance of protein aggregation may be crucial for therapy of
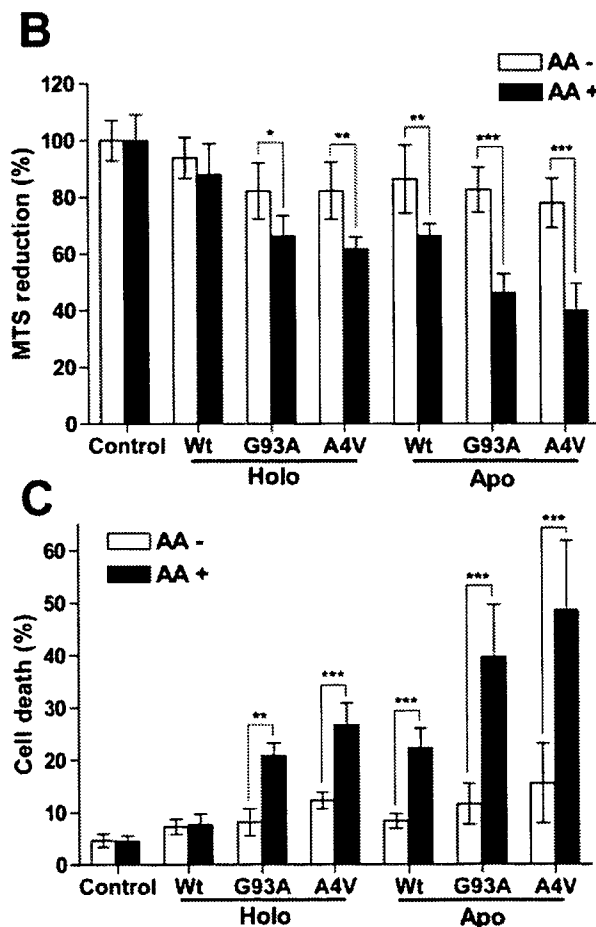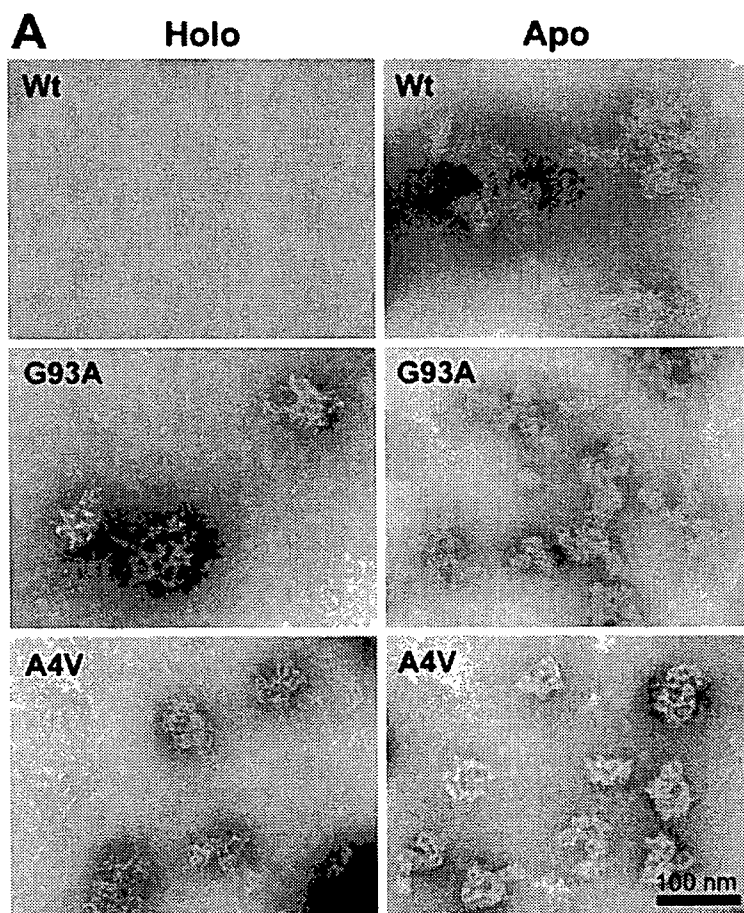
FIG. 7. **SOD1 aggregates and their cytotoxicity for the differentiated neuro2a cells.** Holo-SOD1s were pre-heated at 50 °C for 30 min before incubation with AA. SOD1 proteins (40 μM) were incubated in the presence of 100 μM AA at 37 °C for 24 h before observation under an electron microscope (*A*). Differentiated neuro2a cells were directly exposed for 18 h in medium containing incubated aliquots of SOD1s with or without arachidonic acid. The concentration of SOD1 in the culture medium was 4 μM. Buffer and AA carryover in the culture medium was controlled. Cytotoxicity was assessed using an MTS reduction assay (*B*) and trypan blue exclusion staining (*C*). The results were analyzed by two-way analysis of variance. The values are the means ± S.D. ($n = 6$). *, $p < 0.05$; **, $p < 0.01$; ***, $p < 0.001$.

conformational diseases including FALS.

In the present study, we demonstrated that unsaturated FAs promoted SOD1 oligomerization at physiological pH. SOD1 oligomers were detected by SDS-PAGE under non-reducing conditions. Although immunoreactivity for SOD1 oligomers was decreased in SDS-PAGE under reducing conditions, SOD1 oligomers were considerably SDS-resistant under non-reducing conditions. Based on this method, we found that apo-SOD1 proteins were highly oligomerized by AA compared with holo-SOD1 proteins in time-dependent and FA concentration-dependent manners (Fig. 2, *B* and *C*). Metal-deficient SOD1s may be representative of misfolding intermediates for their oligomeric assemblies because they are oligomerized independent of their mutations. These findings suggest that metal-deficient SOD1 proteins have a high oligomerization propensity, which is consistent with previous studies (9, 10, 13, 32). Moreover, heating of holo-SOD1 mutants increased the tendency to form oligomer complexes, especially in the presence of AA; however, the wild-type holo-SOD1 did not form oligomers, even after heating to 68 °C and exposure to AA (Fig. 5). This finding suggests that mutations of SOD1 primarily affect their conformation. Our time-course analysis of oligomerization demonstrates that FAs induced the oligomerization process fairly rapidly. We could detect oligomers within 1 h of incubation in the presence of AA (Fig. 1C). Glycerol density gradient centrifugation analysis showed that oligomer species were roughly estimated to be >80% of the total SOD1 after a 90-min incubation in the presence of AA (Fig. 4). The conversion efficiency and the speed of oligomer formation may be considered as supportive evidence that these reactions occur *in vivo*.

Aggregations of misfolded proteins are primarily affected by their mutations, especially in inherited conformational diseases. Mutant proteins in conformational diseases have a common characteristic of easily unfolding in a physiological condition and favoring aggregate formation. Protein aggregation has also been shown to be modulated by several factors, including protein concentration, pH, and interactions with other elements such as lipid molecules. It has been reported that FAs stimulated the polymerization of amyloid β-peptides, tau (17, 33), and α-synuclein (18, 19) *in vitro*. These studies suggest that FAs play a pivotal role as nucleates in the self-assembly of misfolded proteins. Although the precise mechanism of how lipid molecules accelerate protein aggregation has not been elucidated, it has been proposed that lipid-bound proteins change their conformation or anionic surfaces, presenting as micelles or vesicles, which can serve to nucleate aggregate formation (18, 34, 35). We confirmed that apo-SOD1s or heat-treated holo-SOD1 mutants were bound to oleic acid (Fig. 6). The FA binding properties of SOD1s were strongly correlated to their conformational instability. These results are consistent with the notion that misfolding intermediates of SOD1 caused by mutations or metal loss may be facilitated by FAs to form oligomeric structures. Another possible mechanism is protein oxidation by FAs. Oxidation also enhances misfolding and aggregation of SOD1 (32). In particular, FAs can lead to the production of radicals because they are easily peroxidized by auto-oxidation to generate peroxyl radicals. However, we could not inhibit SOD1 oligomerization using even a considerable amount of radical scavenger (data not shown). Moreover, oxidized derivatives of FAs also induced SOD1 oligomerization to a similar extent with fresh FAs (data not shown). This finding suggests that oxidation or oxidative damage of SOD1 does not directly drive SOD1 oligomerization. Rather, it is most likely to be associated with a SOD1-destabilizing event.

Recently, several studies for *in vitro* aggregation of SOD1 have been published. Aggregation of SOD1 can be induced by

metal-catalyzed oxidation (32), trifluoroethanol, or heat treatment (10), which induces oxidative modification or protein destabilization. This indicates that structurally unstable SOD1 has an influence on its aggregate formation *in vitro*. Crystallographic studies suggest that metal-deficient SOD1 forms an amyloid-like assembly caused by non-native conformational changes and permits dimer interaction (36, 37). This amyloid-like structure was represented by prolonged incubation of SOD1 at acidic pH (9). In the present study, ultrastructural analysis showed that the FA-inducing aggregates had round or amorphous morphology with clustered tiny spherical aggregates (Fig. 7A). They resemble pre-fibrillar aggregates of the N-terminal domain of *Escherichia coli* HypF protein or aggregates of the Src homology 3 domain of cytosolic phosphatidylinositol 3-kinase as reported by Stefani and co-workers (26). They demonstrated that granular aggregates of proteins, even non-pathological proteins, are cytotoxic when applied externally (26). Our data also demonstrate that granular aggregates of SOD1s reveal significant cytotoxicity (Fig. 7, *B* and *C*). Although the cytotoxic mechanism of the aggregates is not completely understood, it has been proposed that such pre-fibrillar intermediates may lead to cytotoxicity by permeabilization of the membrane bilayer (38, 39).

The present findings may provide considerable pathological implication for FALS. Lipid molecules such as FAs may be positive modulators for misfolded protein aggregations. Most misfolded proteins including SOD1 mutants are rapidly degraded by the ubiquitin-proteasome system. Unsaturated FAs may promote misfolded protein aggregations before they are degraded. In addition, cytotoxic aggregate formation of SOD1 may require FAs because granular aggregates structures were markedly observed in SOD1s incubated with AA. Although it is not clear whether the cytotoxic aggregates of SOD1s are generated intracellularly, we have provided a protein aggregation model system to help understand the pathological significance of FAs as a positive modulator for the aggregate formation in FALS. We believe that our system will contribute to efficient drug screening for inhibitors of SOD1 aggregation.

REFERENCES

1. Deng, H. X., Hentati, A., Tainer, J. A., Iqbal, Z., Cayabyab, A., Hung, W. Y., Getzoff, E. D., Hu, P., Herzfeldt, B., Roos, R. P., Warner, C., Deng, G., Soriano, E., Smyth, C., Parge, H. E., Ahmed, A., Roses, A. D., Hallewell, R., Pericak-Vance, M. A., and Siddique, T. (1993) *Science* **261**, 1047–1051
2. Rosen, D. R., Siddique, T., Patterson, D., Figlewicz, D. A., Sapp, P., Hentati, A., Donaldson, D., Goto, J., O'Regan, J. P., Deng, H. X., Rahmani, Z., Krizus, A., McKenna-Yasek, D., Cayabyab, A., Gaston, S., Tanzi, R., Halperin, J. J., Herzfeldt, B., Van den Berg, R., Hung, W., Bird, T., Deng, G., Mulder, D. W., Smith, C., Laing, N. G., Soriano, E., Pericak-Vance, M. A., Haines, J., Rouleau, G. A., Gusella, J., Horvitz, H. R., and Brown, R. H., Jr. (1993) *Nature* **362**, 59–62
3. Shibata, N., Asayama, K., Hirano, A., and Kobayashi, M. (1996) *Dev. Neurosci.* **18**, 492–498
4. Bruijn, L. I., Becher, M. W., Lee, M. K., Anderson, K. L., Jenkins, N. A., Copeland, N. G., Sisodia, S. S., Rothstein, J. D., Borchelt, D. R., Price, D. L., and Cleveland, D. W. (1997) *Neuron* **18**, 327–338
5. Kato, S., Hayashi, H., Nakashima, K., Nanba, E., Kato, M., Hirano, A., Nakano, I., Asayama, K., and Ohama, E. (1997) *Am. J. Pathol.* **151**, 611–620
6. Shibata, N., Hirano, A., Kobayashi, M., Dal Canto, M. C., Gurney, M. E., Komori, T., Umahara, T., and Asayama, K. (1998) *Acta Neuropathol.* **95**, 136–142
7. Watanabe, M., Dykes-Hoberg, M., Culotta, V. C., Price, D. L., Wong, P. C., and Rothstein, J. D. (2001) *Neurobiol. Dis.* **8**, 933–941
8. Wang, J., Xu, G., Gonzales, V., Coonfield, M., Fromholt, D., Copeland, N. G., Jenkins, N. A., and Borchelt, D. R. (2002) *Neurobiol. Dis.* **10**, 128–138
9. DiDonato, M., Craig, L., Huff, M. E., Thayer, M. M., Cardoso, R. M., Kassmann, C. J., Lo, T. P., Bruns, C. K., Powers, E. T., Kelly, J. W., Getzoff, E. D., and Tainer, J. A. (2003) *J. Mol. Biol.* **332**, 601–615
10. Stathopulos, P. B., Rumfeldt, J. A., Scholz, G. A., Irani, R. A., Frey, H. E., Hallewell, R. A., Lepock, J. R., and Meiering, E. M. (2003) *Proc. Natl. Acad. Sci. U. S. A.* **100**, 7021–7026
11. Hayward, L. J., Rodriguez, J. A., Kim, J. W., Tiwari, A., Goto, J. J., Cabelli, D. E., Valentine, J. S., and Brown, R. H., Jr. (2002) *J. Biol. Chem.* **277**, 15923–15931

12. Rodriguez, J. A., Valentine, J. S., Eggers, D. K., Roe, J. A., Tiwari, A., Brown, R. H., Jr., and Hayward, L. J. (2002) *J. Biol. Chem.* **277,** 15932–15937
13. Lindberg, M. J., Tibell, L., and Oliveberg, M. (2002) *Proc. Natl. Acad. Sci. U. S. A.* **99,** 16607–16612
14. Johnston, J. A., Dalton, M. J., Gurney, M. E., and Kopito, R. R. (2000) *Proc. Natl. Acad. Sci. U. S. A.* **97,** 12571–12576
15. Urushitani, M., Kurisu, J., Tateno, M., Hatakeyama, S., Nakayama, K., Kato, S., and Takahashi, R. (2004) *J. Neurochem.* **90,** 231–244
16. Shinder, G. A., Lacourse, M. C., Minotti, S., and Durham, H. D. (2001) *J. Biol. Chem.* **276,** 12791–12796
17. Wilson, D. M., and Binder, L. I. (1997) *Am. J. Pathol.* **150,** 2181–2195
18. Sharon, R., Goldberg, M. S., Bar-Josef, I., Betensky, R. A., Shen, J., and Selkoe, D. J. (2001) *Proc. Natl. Acad. Sci. U. S. A.* **98,** 9110–9115
19. Sharon, R., Bar-Joseph, I., Frosch, M. P., Walsh, D. M., Hamilton, J. A., and Selkoe, D. J. (2003) *Neuron* **37,** 583–595
20. Urushitani, M., Kurisu, J., Tsukita, K., and Takahashi, R. (2002) *J. Neurochem.* **83,** 1030–1042
21. Fried, R. (1975) *Biochimie (Paris)* **57,** 657–660
22. Crow, J. P., Sampson, J. B., Zhuang, Y., Thompson, J. A., and Beckman, J. S. (1997) *J. Neurochem.* **69,** 1936–1944
23. Boissinot, M., Karnas, S., Lepock, J. R., Cabelli, D. E., Tainer, J. A., Getzoff, E. D., and Hallewell, R. A. (1997) *EMBO J.* **16,** 2171–2178
24. Bartnikas, T. B., and Gitlin, J. D. (2003) *J. Biol. Chem.* **278,** 33602–33608
25. Peters, T., Jr., Taniuchi, H., and Anfinsen, C. B., Jr. (1973) *J. Biol. Chem.* **248,** 2447–2451
26. Bucciantini, M., Giannoni, E., Chiti, F., Baroni, F., Formigli, L., Zurdo, J., Taddei, N., Ramponi, G., Dobson, C. M., and Stefani, M. (2002) *Nature* **416,** 507–511
27. Kayed, R., Head, E., Thompson, J. L., McIntire, T. M., Milton, S. C., Cotman, C. W., and Glabe, C. G. (2003) *Science* **300,** 486–489
28. Kato, S., Saito, M., Hirano, A., and Ohama, E. (1999) *Histol. Histopathol.* **14,** 973–989
29. Walsh, D. M., Hartley, D. M., Kusumoto, Y., Fezoui, Y., Condron, M. M., Lomakin, A., Benedek, G. B., Selkoe, D. J., and Teplow, D. B. (1999) *J. Biol. Chem.* **274,** 25945–25952
30. Hartley, D. M., Walsh, D. M., Ye, C. P., Diehl, T., Vasquez, S., Vassilev, P. M., Teplow, D. B., and Selkoe, D. J. (1999) *J. Neurosci.* **19,** 8876–8884
31. Tateno, M., Sadakata, H., Tanaka, M., Itohara, S., Shin, R. M., Miura, M., Masuda, M., Aosaki, T., Urushitani, M., Misawa, H., and Takahashi, R. (2004) *Hum. Mol. Genet.* **13,** 2183–2196
32. Rakhit, R., Cunningham, P., Furtos-Matei, A., Dahan, S., Qi, X. F., Crow, J. P., Cashman, N. R., Kondejewski, L. H., and Chakrabartty, A. (2002) *J. Biol. Chem.* **277,** 47551–47556
33. Gamblin, T. C., King, M. E., Kuret, J., Berry, R. W., and Binder, L. I. (2000) *Biochemistry* **39,** 14203–14210
34. Necula, M., Chirita, C. N., and Kuret, J. (2003) *J. Biol. Chem.* **278,** 46674–46680
35. Chirita, C. N., Necula, M., and Kuret, J. (2003) *J. Biol. Chem.* **278,** 25644–25650
36. Elam, J. S., Taylor, A. B., Strange, R., Antonyuk, S., Doucette, P. A., Rodriguez, J. A., Hasnain, S. S., Hayward, L. J., Valentine, J. S., Yeates, T. O., and Hart, P. J. (2003) *Nat. Struct. Biol.* **10,** 461–467
37. Strange, R. W., Antonyuk, S., Hough, M. A., Doucette, P. A., Rodriguez, J. A., Hart, P. J., Hayward, L. J., Valentine, J. S., and Hasnain, S. S. (2003) *J. Mol. Biol.* **328,** 877–891
38. Caughey, B., and Lansbury, P. T. (2003) *Annu. Rev. Neurosci.* **26,** 267–298
39. Kayed, R., Sokolov, Y., Edmonds, B., McIntire, T. M., Milton, S. C., Hall, J. E., and Glabe, C. G. (2004) *J. Biol. Chem.* **279,** 46363–46366

Essential role for autophagy protein Atg7 in the maintenance of axonal homeostasis and the prevention of axonal degeneration

Masaaki Komatsu[*†‡], Qing Jun Wang[§¶], Gay R. Holstein[¶], Victor L. Friedrich, Jr.[¶], Jun-ichi Iwata[*†], Eiki Kominami[†], Brian T. Chait[§], Keiji Tanaka[*], and Zhenyu Yue[¶‖]

[¶]Departments of Neurology and Neuroscience, Mount Sinai School of Medicine, New York, NY 10029; [*]Laboratory of Frontier Science, Tokyo Metropolitan Institute of Medical Science, Bunkyo-ku, Tokyo 113-8613, Japan; [†]Department of Biochemistry, Juntendo University School of Medicine, Bunkyo-ku, Tokyo 113-8421, Japan; [‡]Precursory Research for Embryonic Science and Technology, Japan Science and Technology Corporation, Kawaguchi 332-0012, Japan; and [§]Laboratory of Mass Spectrometry and Gaseous Ion Chemistry, Rockefeller University, New York, NY 10065

Autophagy is a regulated lysosomal degradation process that involves autophagosome formation and transport. Although recent evidence indicates that basal levels of autophagy protect against neurodegeneration, the exact mechanism whereby this occurs is not known. By using conditional knockout mutant mice, we report that neuronal autophagy is particularly important for the maintenance of local homeostasis of axon terminals and protection against axonal degeneration. We show that specific ablation of an essential autophagy gene, Atg7, in Purkinje cells initially causes cell-autonomous, progressive dystrophy (manifested by axonal swellings) and degeneration of the axon terminals. Consistent with suppression of autophagy, no autophagosomes are observed in these dystrophic swellings, which is in contrast to accumulation of autophagosomes in the axonal dystrophic swellings under pathological conditions. Axonal dystrophy of mutant Purkinje cells proceeds with little sign of dendritic or spine atrophy, indicating that axon terminals are much more vulnerable to autophagy impairment than dendrites. This early pathological event in the axons is followed by cell-autonomous Purkinje cell death and mouse behavioral deficits. Furthermore, ultrastructural analyses of mutant Purkinje cells reveal an accumulation of aberrant membrane structures in the axonal dystrophic swellings. Finally, we observe double-membrane vacuole-like structures in wild-type Purkinje cell axons, whereas these structures are abolished in mutant Purkinje cell axons. Thus, we conclude that the autophagy protein Atg7 is required for membrane trafficking and turnover in the axons. Our study implicates impairment of axonal autophagy as a possible mechanism for axonopathy associated with neurodegeneration.

axon | axonopathy | neurodegeneration | autophagosome | Purkinje cell

Macroautophagy is characterized by dynamic membrane rearrangements, involving the formation, trafficking, and degradation of double-membrane autophagic vacuoles (autophagosomes) in the cytoplasm. Macroautophagy (hereafter referred to as autophagy) is a highly regulated process, which can be induced by nutrient starvation, trophic factors, and stress (1). Despite recent advances in characterizing autophagy in several model systems, autophagic processes in the nervous system remain poorly understood. On one hand, nutrient deprivation has not been observed to induce autophagy in the mammalian brain (2), thus suggesting a specific regulatory system for autophagy that is not typically activated by starvation. On the other hand, a variety of conditions that cause neuronal stress or degeneration can lead to the accumulation of autophagosomes in neurons, thus implicating autophagy in these neuropathogenic processes (3, 4).

The axon is a highly specialized neuronal compartment that performs many functions independently from the cell body. After axotomy or excitotoxicity, double-membrane vacuoles resembling autophagosomes were originally observed to accumulate in dilated axon terminals that result from the injury (5, 6), a local phenomenon that is not observed in undisturbed axons. Autophagosome-like vacuoles have also been shown to be present in the dysfunctional or degenerating axons associated with a range of chronic neurodegenerative conditions, including Alzheimer's (7, 8), Parkinson's (9), Huntington's (10), and Creutzfeldt–Jakob (11) diseases and their animal models (12–14). These observations suggest a link between locally altered autophagy and axonopathy, which is one of the underlying mechanisms in neurodegeneration (15).

Although the biological significance of these autophagosomes-like vacuoles in degenerating axons is unclear, recent studies have shown that genetic inactivation of autophagy in the mouse CNS causes neurodegeneration accompanied by axonal dystrophy and the formation of intracellular ubiquitin-associated inclusions (16, 17). These studies suggest a role for basal levels of autophagy in neuronal protection and in protein quality control. However, the connection between the inactivation of autophagy and the observed axonal dystrophy and neurodegeneration remains to be determined. In addition, because autophagy was suppressed in all cell types in the CNS (including neurons and nonneuronal cells) (16, 17), it is not known whether the observed axonal dystrophy and neurodegeneration is cell-autonomous.

Here, we seek to further elucidate the physiological function of neuronal autophagy by generating conditional knockout mice with Purkinje cell-specific deletion of Atg7, an autophagy gene encoding E1-like enzyme in the two ubiquitin-like conjugation systems that are essential for the autophagosome biogenesis (18). We show that ablation of Atg7 leads to abnormal swellings and dystrophy of Purkinje cell axon terminals in the deep cerebellar nuclei (DCN). Subsequently, these Atg7-deletion mice develop cell-autonomous neurodegeneration of Purkinje cells, dendritic atrophy, and behavioral deficits. Moreover, double-membrane vacuole-like structures are formed in the distal ends of wild-type Purkinje cell axons, whereas they are absent in Atg7-deletion Purkinje cell axons.
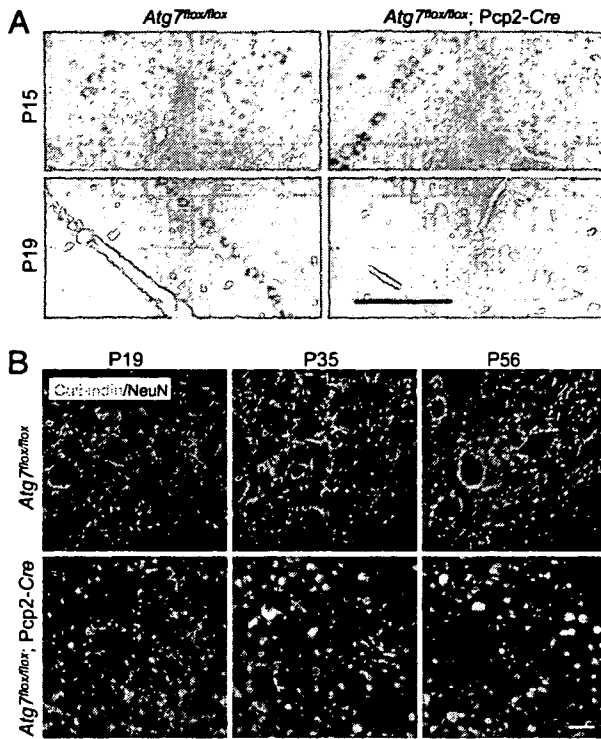
A

B

Fig. 1. Deletion of Atg7 specifically in Purkinje cells caused progressive dystrophic swelling of axon terminals. (A) Immunohistochemistry of Atg7 protein expression in Purkinje cells of Atg7$^{flox/flox}$ and Atg7$^{flox/flox}$;Pcp2-Cre mice at P15 and P19. The endogenous Atg7 protein was present at P15 but absent at P19 in the Atg7$^{flox/flox}$;Pcp2-Cre Purkinje cells. (Scale bar: 100 μm.) (B) Progression of the abnormal Purkinje cell axon terminal swellings in the DCN of Atg7$^{flox/flox}$;Pcp2-Cre mice (anti-calbindin immunofluorescent staining in green with anti-NeuN counterstained in red) at P19, P35, and P56. Atg7$^{flox/flox}$ was used as control. (Scale bar: 20 μm.) n = 3–5.

Instead, the mutant Purkinje cell axon terminal swellings accumulate aberrant membranous structures. Our results suggest that autophagy is required for normal axon terminal membrane trafficking and turnover, and indicate an essential role of local autophagy in the maintenance of axonal homeostasis and prevention of axonal degeneration.

Results

Specific Depletion of Atg7 in Purkinje Cells Caused Cell-Autonomous Dystrophy and Degeneration of Axon Terminals.

To generate Purkinje cell-specific deletion of Atg7 in mice, we crossed mice harboring the floxed Atg7 alleles (19) with transgenic mice expressing Cre recombinase under control of the Pcp2 (L7) promoter (20) to establish the mouse line Atg7$^{flox/flox}$;Pcp2-Cre. To determine when loss of the endogenous Atg7 protein occurred, we examined Atg7 expression in Atg7$^{flox/flox}$;Pcp2-Cre mice at postnatal day 15 (P15) and P19. At P15, Atg7 was expressed at similar levels in Purkinje cells of both mutant Atg7$^{flox/flox}$;Pcp2-Cre and the control Atg7$^{flox/flox}$ mice, whereas at P19, despite residual expression in a small number of Purkinje cells (<12%), Atg7 immunostaining was largely diminished in Atg7$^{flox/flox}$;Pcp2-Cre Purkinje cells (>88%), but unchanged in the Atg7$^{flox/flox}$ Purkinje cells (Fig. 1A). At P35, >95% Purkinje cells in Atg7$^{flox/flox}$;Pcp2-Cre showed no detectable Atg7 expression (data not shown). In addition, Atg7 deficiency in Atg7$^{flox/flox}$;Pcp2-Cre mice was specific for Purkinje cells because Atg7 is clearly present in the other cell types (Fig. 1A). Thus, the specific loss of Atg7 in Purkinje cells occurred largely between P15 and P19 in Atg7$^{flox/flox}$;Pcp2-Cre mice.

Next, we examined Purkinje cell axons in the DCN of

Atg7$^{flox/flox}$;Pcp2-Cre mice by immunofluorescent staining using an antibody against calbindin, a Purkinje cell marker. At P15, no morphological alteration was observed in the axons of Atg7$^{flox/flox}$;Pcp2-Cre Purkinje cells compared with those of Atg7$^{flox/flox}$ Purkinje cells [supporting information (SI) Fig. 7], consistent with the presence of normal levels of Atg7 in Atg7$^{flox/flox}$;Pcp2-Cre Purkinje cells at this stage (Fig. 1A). However, at P19, Atg7$^{flox/flox}$;Pcp2-Cre Purkinje cell axons were abnormally dilated, as visualized by green fluorescence-labeled "endbulbs" (Fig. 1B). In addition, these Purkinje cell axonal swellings were labeled with the antibody raised against synaptophysin, the presynaptic terminal marker (SI Fig. 8), suggesting that they were terminals of Purkinje cell axons. The number and size of the swollen axon terminals in the DCN of the Atg7$^{flox/flox}$;Pcp2-Cre were markedly increased at P35 in comparison with those at P19 (Fig. 1B). At P56, the number of such axonal dystrophic swellings of the mutant Purkinje cells was noticeably decreased in comparison with that at P35, suggesting that many of these swollen axons had degenerated by this age (Fig. 1B). These data demonstrated that deletion of Atg7 caused cell-autonomous axonal dystrophy and degeneration in Purkinje cells.

Axonal Dystrophic Swellings of Atg7$^{flox/flox}$;Pcp2-Cre Purkinje Cells Were Devoid of GFP-Light Chain 3 (LC3)-Labeled Puncta and Exhibited Increased Levels of p62/SQSTM1.

Transgenic mice producing GFP fused with microtubule-associated protein 1 light chain 3 (LC3), a specific marker for autophagosomes (21), were previously generated to monitor autophagosomes in vivo (2). By expressing GFP-LC3 in Lurcher mice (GFP-LC3/Lurcher), we showed that a large number of autophagosomes were formed in the dystrophic axon terminals of Lurcher Purkinje cells (Fig. 2Ad), providing in vivo evidence for the induction of autophagy in response to Lurcher-induced excitotoxicity (22). To assess autophagic activity in the dystrophic axons of Atg7$^{flox/flox}$;Pcp2-Cre Purkinje cells, we crossed transgenic GFP-LC3 with Atg7$^{flox/flox}$;Pcp2-Cre mice (Atg7$^{flox/flox}$;Pcp2-Cre/GFP-LC3). Despite intense GFP-LC3 accumulation in the axonal dystrophic swellings of Purkinje cells in Atg7$^{flox/flox}$;Pcp2-Cre/GFP-LC3 mice at P35, no GFP-LC3 fluorescent puncta characteristic of autophagosomes were observed in these swellings (Fig. 2A b and c). We contrasted this finding to our observation of GFP-LC3 puncta in Purkinje cell axons GFP-LC3/Lurcher mice (Fig. 2Ad) (22). In addition, no GFP-LC3 puncta were observed in the somata or dendrites of Atg7$^{flox/flox}$;Pcp2-Cre/GFP-LC3 Purkinje cells (Fig. 2A f and g), again in contrast to the observation of GFP-LC3 puncta in the somata and dendrites of GFP-LC3/Lurcher Purkinje cells (Fig. 2Ah) (22).

It has been shown that inhibition of autophagy is correlated with increased levels of the polyubiquitin binding protein p62/SQSTM1 (22, 23). We thus examined the levels of p62/SQSTM1 in Atg7$^{flox/flox}$;Pcp2-Cre Purkinje cells. As detected with anti-p62/SQSTM1 immunofluorescent staining, p62/SQSTM1 was markedly accumulated in the axonal dystrophic swellings (Fig. 2B, arrows) and somata (SI Fig. 9) of Atg7$^{flox/flox}$;Pcp2-Cre Purkinje cells in comparison with Atg7$^{flox/flox}$ Purkinje cells. It is also noteworthy that the dystrophic axonal swellings in Lurcher Purkinje cells did not have detectable p62/SQSTM1 immunofluorescent staining (SI Fig. 10). These results provided molecular evidence for impaired autophagic activity in the dystrophic axons of Atg7$^{flox/flox}$;Pcp2-Cre Purkinje cells, but not in the dystrophic axons of Lurcher Purkinje cells.

Atg7$^{flox/flox}$;Pcp2-Cre Purkinje Cells Exhibited Normal Dendritic Tree and Spine Morphology at P56.

Despite the remarkable dystrophy and degeneration of Purkinje cell axon terminals in the DCN of Atg7$^{flox/flox}$;Pcp2-Cre mice at P35 and P56, the cerebellar cortex displayed little change in its overall size and organization (Fig. 3A). For example, at P35 and P56, Atg7$^{flox/flox}$;Pcp2-Cre mice and
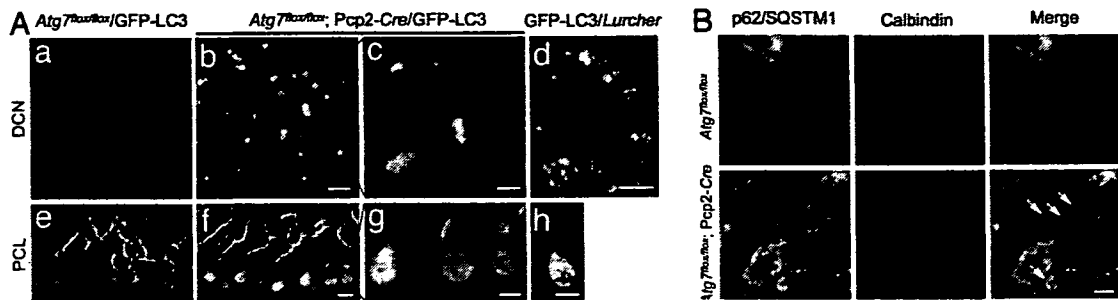
Fig. 2. The axonal dystrophic swellings of the Atg7-deficient Purkinje cells contained no GFP-LC3 labeled autophagosomes but accumulated p62/SQSTM1. (A) The absence of GFP-LC3 puncta in Purkinje cell axonal dystrophic swellings (b and c) and somata (f and g) of Atg7$^{flox/flox}$;Pcp2-Cre/GFP-LC3 mice (P35). GFP-LC3 puncta were found in GFP-LC3/Lurcher Purkinje cell axonal dystrophic swellings (d) and somata (h) (P12). DCN (a) and Purkinje cell layer (PCL) (e) of control mice Atg7$^{flox/flox}$/GFP-LC3 are shown. (Scale bars: a, b, e, and f, 20 μm; c, d, g, and h, 10 μm.) (B) Anti-p62/SQSTM1 immunofluorescent staining (in green) showed accumulation of p62/SQSTM1 in Purkinje cell axonal dystrophic swellings (calbindin labeling in red) (white arrows) in the DCN of Atg7$^{flox/flox}$;Pcp2-Cre mice at P56. Atg7$^{flox/flox}$ was used as control. (Scale bar: 10 μm.)

Atg7$^{flox/flox}$ mice did not exhibit significant difference in their cerebellar molecular layer thickness (Fig. 3A and B). To evaluate changes in dendritic tree and spine morphology, we examined the expression pattern of metabotropic glutamate receptor 1α (mGluR1α) protein, a marker for parallel fiber–Purkinje cell synapses. No difference in localization and intensity of the anti-mGluR1α immunofluorescent staining was observed between the Atg7$^{flox/flox}$;Pcp2-Cre and Atg7$^{flox/flox}$ cerebellar molecular layers at either P35 (data not shown) or P56 (Fig. 3C). Thus, Atg7 deletion had little effect on Purkinje cell dendritic tree and spine morphology up to at least P56. We conclude that Atg7
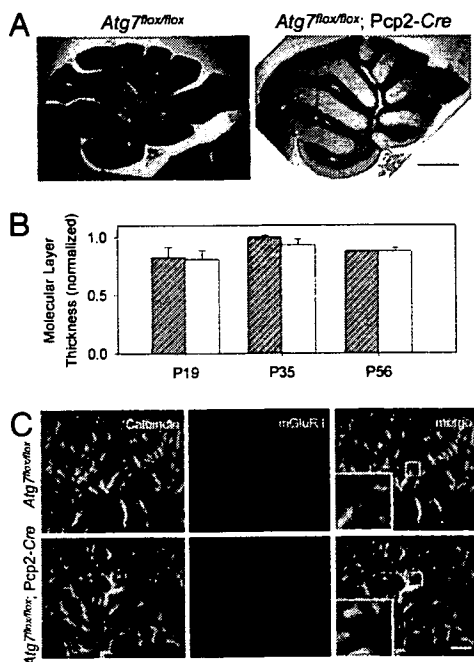

Fig. 3. Deletion of Atg7 in Purkinje cells had little effect on the morphology of cerebellar cortex, Purkinje cell dendritic tree and spines in Atg7$^{flox/flox}$;Pcp2-Cre mice at P56. (A) H&E-stained images of midsagittal sections from Atg7$^{flox/flox}$ and Atg7$^{flox/flox}$;Pcp2-Cre cerebella at P56. (Scale bar: 0.5 mm.) n = 3–5. (B) Quantification of the molecular layer thickness (as the distance between lobules V and VI of the Purkinje cell layer divided by 2) from the cerebellar midsagittal sections of Atg7$^{flox/flox}$ and Atg7$^{flox/flox}$;Pcp2-Cre mice at P19, P35, and P56. n = 3–5. (C) Immunofluorescent staining of cerebellar midsagittal sections shows normal localization and appearance of mGluR1α (in red) in Atg7$^{flox/flox}$;Pcp2-Cre mice compared with Atg7$^{flox/flox}$ mice at P56. Green indicates anti-calbindin. (Scale bar: 10 μm.) n = 3.
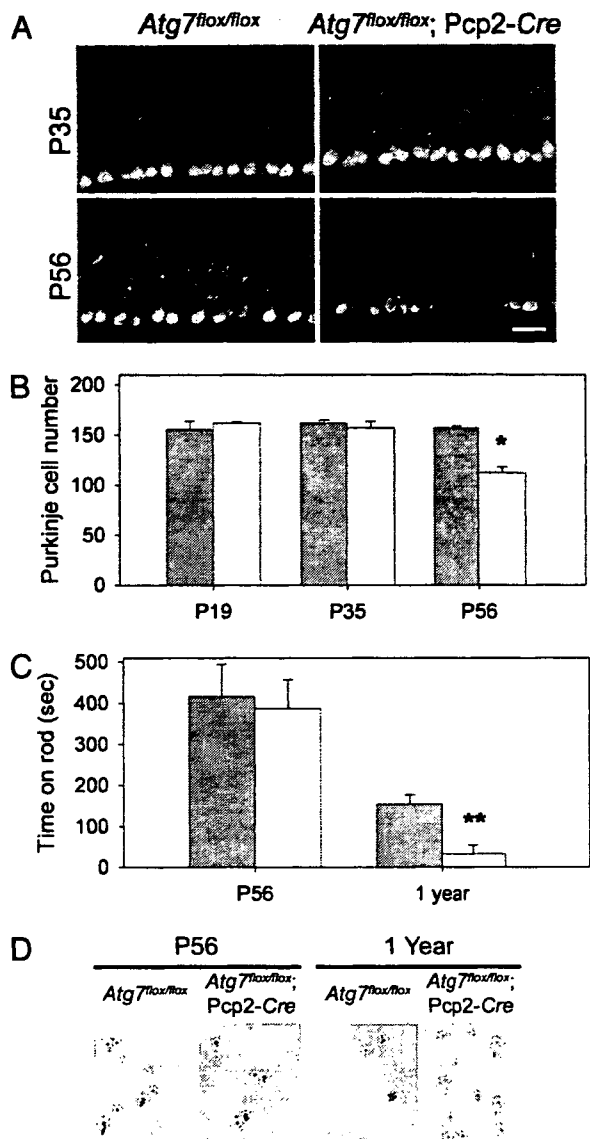
deletion in Purkinje cells elicit differential effects on the dendritic and axonal compartments, suggesting that the axon terminals are particularly vulnerable to autophagy deficiency.

Axonal Dystrophy Preceded Cell-Autonomous Degeneration of Purkinje Cells and Behavioral Deficits in Atg7$^{flox/flox}$;Pcp2-Cre Mice. To further evaluate the effects of Atg7 deletion, we assayed for Purkinje cell degeneration and mouse behavioral deficits. Whereas the Purkinje cell axonal dystrophic swellings in the DCN of Atg7$^{flox/flox}$;Pcp2-Cre mice first became apparent at P19 and grew severe at P35 (Fig. 2A), no significant difference in Purkinje cell numbers was observed between the Atg7$^{flox/flox}$;Pcp2-Cre and Atg7$^{flox/flox}$ mice at both ages (Fig. 4A and B). However, at P56, the number of Purkinje cells in Atg7$^{flox/flox}$;Pcp2-Cre mice was reduced by 28.4% (P < 0.0005) compared with Atg7$^{flox/flox}$ mice (Fig. 4A and B). Thus, loss of Purkinje cells in Atg7$^{flox/flox}$;Pcp2-Cre mice occurred between P35 and P56. In comparison, the onset of axonal dystrophy began as early as P19. In addition, levels of GluRδ2 (a Purkinje cell-specific glutamate receptor subtype) in Atg7$^{flox/flox}$;Pcp2-Cre cerebellar extract were not reduced until P56 (SI Fig. 11), further supporting that the onset of axon dystrophy was earlier than Purkinje cell degeneration in Atg7$^{flox/flox}$;Pcp2-Cre mice.

Next, we assessed the locomotive behaviors in Atg7$^{flox/flox}$;Pcp2-Cre mice by limb-clasping, rotarod, and gait analyses at different postnatal ages. At P19 and P35, Atg7$^{flox/flox}$;Pcp2-Cre mice appeared normal and did not show any difference in performance compared with their control Atg7$^{flox/flox}$ littermates (data not shown). At P56, Atg7$^{flox/flox}$;Pcp2-Cre and Atg7$^{flox/flox}$ mice performed equally well on the rotarod and gait analyses (Fig. 4 C and D). However, 5 of 13 Atg7$^{flox/flox}$;Pcp2-Cre mice (38.5%) displayed limb-clasping reflexes on tail suspension, in comparison with 0 of 10 of their control littermates (P < 0.01). Thus, at P56, despite the 28.4% loss of Purkinje cells (Fig. 4B), Atg7$^{flox/flox}$;Pcp2-Cre mice displayed only mild behavioral impairment. In contrast, at 1 year, these mice demonstrated severe behavioral disorders in locomotion and motor coordination when evaluated in all three behavioral tests (Fig. 4 C and D; data not shown).

We summarize the temporal relationship of the morphological alterations, differential pathology in different compartments of Purkinje cells, and behavioral changes in Atg7$^{flox/flox}$;Pcp2-Cre mice in SI Table 1. These results demonstrate that axonal dystrophic swelling is an early pathogenic event and is likely to be a direct result of impairment of local autophagy in axon terminals.

Aberrant Membrane Structures Accumulated in the Dystrophic Axon Terminals of Atg7$^{flox/flox}$;Pcp2-Cre Purkinje Cells. To further assess the effect of impairment of autophagy on axon terminals, we characterized the axonal dystrophic swellings of Atg7$^{flox/flox}$;Pcp2-

A Atg7$^{flox/flox}$ Atg7$^{flox/flox}$; Pcp2-Cre

P35

P56

B
Purkinje cell number
200
150
100
50
0
P19   P35   P56
*

C
Time on rod (sec)
500
400
300
200
100
0
P56   1 year
**   ***

D   P56   1 Year

Atg7$^{flox/flox}$ Atg7$^{flox/flox}$; Pcp2-Cre   Atg7$^{flox/flox}$ Atg7$^{flox/flox}$; Pcp2-Cre

Fig. 4. Time course of Purkinje cell degeneration and locomotive behavioral deficits in Atg7$^{flox/flox}$;Pcp2-Cre mice. (A) Anti-calbindin immunofluorescent staining of the cerebellar midsagittal sections of Atg7$^{flox/flox}$ and Atg7$^{flox/flox}$;Pcp2-Cre mice at P35 and P56. (B) Quantitation of Purkinje cells at lobules IV–V of the midsagittal sections of Atg7$^{flox/flox}$ and Atg7$^{flox/flox}$;Pcp2-Cre mice at P19, P35, and P56 based on H&E-stained images. n = 3, 3, and 3 for Atg7$^{flox/flox}$ at P19, P35, and P56, respectively. n = 2, 3, and 5 for Atg7$^{flox/flox}$;Pcp2-Cre at P19, P35, and P56, respectively (*, $P < 0.0005$). (C) At P56, Atg7$^{flox/flox}$ and Atg7$^{flox/flox}$;Pcp2-Cre mice showed no significant difference in the time spent on the rod in rotarod assay. At 1 year, Atg7$^{flox/flox}$ mice spent much longer time on the rod than Atg7$^{flox/flox}$;Pcp2-Cre mice (**, $P < 0.05$). (D) In gait analyses at P56, Atg7$^{flox/flox}$ and Atg7$^{flox/flox}$;Pcp2-Cre mice showed similar step width and overlapping of forefeet and hindfeet (forefeet, red; hindfeet, black). At 1 year old, Atg7$^{flox/flox}$;Pcp2-Cre mice showed shorter step width than Atg7$^{flox/flox}$ mice as well as nonoverlapping forefeet and hindfeet (left feet, black; right feet, red). For both C and D, n = 5 at P56; n = 3 and 4 at 1 year.

Cre Purkinje cells by transmission electron microscopy. The cross-sections of the Purkinje cell axon terminals in the DCN of the Atg7$^{flox/flox}$ mice were normally 0.5–2 μm in diameter (Fig. 5A, white arrows). Remarkably, the swollen Purkinje cell axon terminals in the DCN of the Atg7$^{flox/flox}$;Pcp2-Cre mice often spanned 1–6 μm in diameter (Fig. 5 B–F, black arrows) and differed profoundly in their morphology from the axonal dystrophic swellings observed in Lurcher Purkinje cells (Fig. 5G,

black arrows). The Purkinje cell axonal dystrophic swellings of Lurcher mice contained a large number of autophagosomes/autolysosomes (Fig. 5G), whereas those of the Atg7$^{flox/flox}$;Pcp2-Cre mice were devoid of autophagosomes (Fig. 2 and 6Af). However, these autophagasome-free swellings of the Atg7$^{flox/flox}$;Pcp2-Cre Purkinje cell axons often contained abnormal organelles or membrane structures (Fig. 5 B–F, white arrows), including stacks of cisternal membranes that formed lamellar bodies (Fig. 5 B and E, white arrows) (24), large and elaborate cisternal arrays and filaments (Fig. 5F, white arrow), and highly convoluted double-membrane whorls that occupied 1.5–2 μm of the swollen terminal (Fig. 5 C and D, white arrows). The exact nature of these aberrant structures was not clear; they were rarely seen in the somata of Atg7$^{flox/flox}$;Pcp2-Cre Purkinje cells (data not shown) or in the Atg7$^{flox/flox}$ Purkinje cells axons (Fig. 5A). However, it is noteworthy that the formation of convoluted membrane whorls was previously described in hepatocytes with Atg7 deletion and was attributed to a failure in autophagic degradation (19). Our observations suggest a conserved function for autophagy in the clearance of cellular membranes and/or lipids in both axon terminals and hepatocytes.

Vacuole-Like Structures with Double Membranes Were Formed in Normal Purkinje Cell Axons but Were Absent in the Dystrophic Axon Terminals of Atg7$^{flox/flox}$;Pcp2-Cre Purkinje Cells. Interestingly, through further ultrastructural analysis, we observed vacuole-like structures with double membranes in the myelinated Purkinje cell axons in the DCN of control Atg7$^{flox/flox}$ mice (Fig. 6Aa and SI Fig. 12). These structures typically appeared to be closed and had diameters of 0.1–0.5 μm (Fig. 6Aa). We occasionally observed these double-membrane vacuole-like structures in the process of formation (Fig. 6A b–e and SI Fig. 12A). Many of these developing double-membrane vacuole-like structures appeared to be formed through invagination of the axolemma along the myelinated layers (Fig. 6A b and c, SI Fig. 12A), reminiscent of invasion by oligodendrocytic processes (25, 26). Some of them appear to be continuous with the axonal plasma membrane (Fig. 6A d and e), which are enwrapping portions of axoplasm (27). The average number of these distinct double-membrane vacuole-like structures (both closed and in the process of formation) in Purkinje cell axons of Atg7$^{flox/flox}$ mice was ≈0.9/50 μm^2 (Fig. 6B). In contrast, these structures were virtually absent in the Atg7$^{flox/flox}$;Pcp2-Cre mice (Fig. 6 Af, B, and C). Although we have yet to determine the exact nature of the vacuole-like structures with double membranes and their relationship with autophagosomes, our results suggested that Atg7 was required for the formation of these distinct structures in axon terminals of normal Purkinje cells.

Discussion

Axonal dystrophic swelling is a hallmark of CNS axonopathy, which can be triggered by neuronal injuries, excitotoxicity, and various neurodegenerative conditions. Despite the prevalence of this pathology, the molecular mechanisms underlying axonopathy as well as the connection between axonopathy and neurodegeneration remain poorly understood (28). A critical question is whether axonal dystrophy and degeneration precede neuronal cell death or are secondary to neurodegeneration. Here, we analyzed the time course of pathological events after the deletion of the autophagy gene Atg7 in cerebellar Purkinje cells. We showed that axonal dystrophy and degeneration caused by ablation of Atg7 occurred much earlier than the onset of neuronal death, indicating that axonal dystrophy was not secondary to neurodegeneration. In addition, axonal dystrophy and degeneration was a cell-autonomous event, which precluded the action of glia as the primary cause of the axonal dystrophy in Atg7$^{flox/flox}$;Pcp2-Cre mice. Although this study was limited to Purkinje cells for the purpose of cell type-specific study of autophagy, axonal dystrophies occurred widely in many
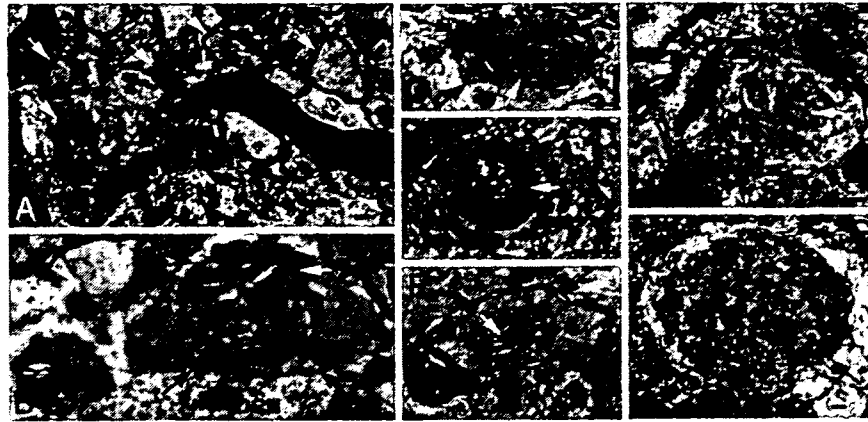
Fig. 5. Deletion of Atg7 in Purkinje cells led to aberrant membrane structures in the axonal dystrophic swellings. Ultrastructural image of normal myelinated Purkinje cell axons (white arrows) and axon terminals (black arrows) in the DCN of Atg7$^{flox/flox}$ mice (A) and Purkinje cell axonal dystrophic swellings (black arrows) in the DCN of Atg7$^{flox/flox}$;Pcp2-Cre mice (B–F). (B and E) Stacks of cisternal membranes (white arrows). (C and D) Convoluted double-membrane whorls (white arrows). (F) The arrays of abnormal filaments (white arrows). (G) A dystrophic axon (black arrows) of Lurcher Purkinje cells containing numerous autophagosomes. (Scale bars: 500 nm.)

regions of the mutant mouse brain with Atg7 or Atg5 deletion (16, 17). We speculate that the axonal dystrophy associated with various types of neurons in these mutant mice are also cell-autonomous events caused by the absence of neuronal autophagy. Importantly, our results implied that interference in local autophagy would have a deleterious effect on axons, a potential mechanism of axonopathies involving impaired autophagy. Furthermore, we showed that deletion of Atg7 had little effect on the overall morphology of the Purkinje cell dendritic arbors at a stage when axon terminals displayed massive dystrophy and degeneration. These differential effects of Atg7 deletion suggested that basal levels of autophagy played a particularly important role in housekeeping functions in axon terminals and in protection against axonal degeneration.

We showed that Atg7 was indispensable for the formation of the distinctive vacuole-like structures with double membranes, which were normally present within wild-type Purkinje cell axons. These structures have not been described previously in the wild-type Purkinje cell axons. Although the majority of these structures were likely derived from invagination of neighboring oligodendrocytes (Fig. 6A b and c and SI Fig. 12A) (25, 26), some of them appeared

to originate from axonal subsurface cisternae (27) or smooth endoplasmic reticulum (29) (Fig. 6A d and e). Although we have yet to determine the nature of these structures, we cannot exclude the possibility that some of these structures are autophagosome-related vacuoles. A previous study has shown the presence and transport of autophagosomes in the axons of cultured sympathetic neurons, despite that the physiological function of autophagy in the axons is unknown (30). Regardless of the nature of these vacuole-like structures, Atg7 deletion abolished their formation, and caused axonal swelling and accumulation of aberrant membrane structures in these swellings. These results established an important role of Atg7 in regulating local membrane trafficking and turnover. However, an important question arising from these results is whether the requirement of Atg7 for the formation of the double-membrane vacuole-like structures is somehow connected to autophagy or associated with a specific Atg7 function independent of autophagy. Current evidence suggests that Atg7 function is exclusively associated with autophagy. Consistent with this idea, the abolishment of the double-membrane vacuole-like structures caused by Atg7 deletion can be explained by the failure of autophagy, which would
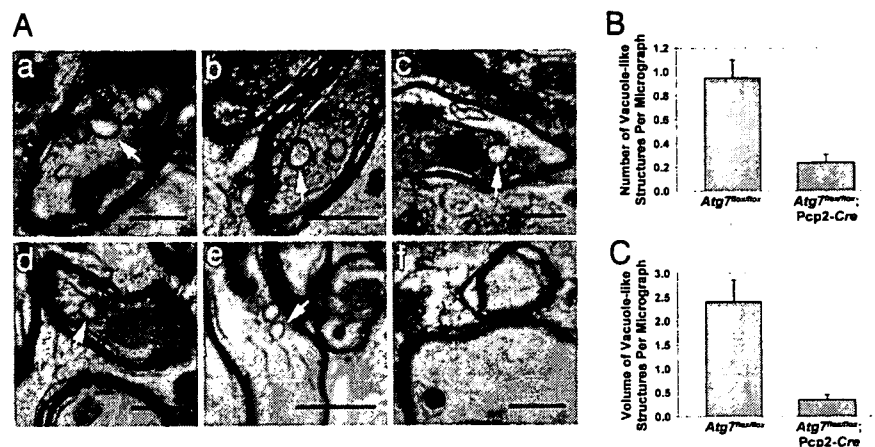

Fig. 6. Deletion of Atg7 in Purkinje cells abolished double-membrane vacuole-like structures in their axon terminals in the DCN. (A) Ultrastructural images show the presence of vacuole-like structures with double membranes in Purkinje cell preterminal axons of Atg7$^{flox/flox}$ mice (a–e, white arrows) and the abolishment of these structures in Atg7$^{flox/flox}$;Pcp2-Cre mice (f) at P35. (Scale bars: 0.5 μm.) (B) Comparison of the numbers of these vacuole-like structures per transmission electron microscopy micrograph (50 μm^2) in the DCN of Atg7$^{flox/flox}$;Pcp2-Cre versus Atg7$^{flox/flox}$ mice (ratio, 4.0; P = 0.00003). (C) Comparison of the volume fraction of double-membrane vacuole-like structures by point counting of transmission electron microscopy micrographs in the DCN of Atg7$^{flox/flox}$;Pcp2-Cre versus Atg7$^{flox/flox}$ mice (ratio, 6.9; P = 0.00002).

normally participate in the formation of these structures. Thus, we hypothesize that, in addition to the role in protein quality control (16, 17), neuronal autophagy regulates membrane homeostasis in the axon terminals. Furthermore, we showed that deletion of *Atg7* caused the axonal terminal swelling, which was a reminiscence of hepatic cell swelling in *Atg7*-deleted mouse liver (19). It is conceivable that axon terminals and hepatocytes may share a similar mechanism for cell (or cellular compartment) size control, which requires autophagy (31).

Previous morphological studies have consistently shown the presence of large numbers of autophagosome-like vacuoles in axonal dystrophic swellings of injured neurons (4–13). We have previously demonstrated that induction of autophagy in *Lurcher* Purkinje cells involved accumulation of autophagosomes in the dystrophic axons (22). In contrast, our present study shows that the axonal swellings of Purkinje cells in *Atg7*$^{flox/flox}$;*Pcp2-Cre* mice were devoid of vacuoles that resembled the autophagosomes observed in *Lurcher* mice. Although our present study demonstrates a role for basal levels of autophagy in axonal protection and indicates that altered autophagy could serve as an adaptive response for remodeling the axon terminals for regeneration (3, 22), we cannot exclude the possibility that up-regulation of autophagy in dystrophic axons is actually destructive, causing overdegradation of axonal structures. This possibility can be tested, in principle, by genetic crossing of the autophagy-deficient mice with diseased mice containing the autophagosome-like vacuoles in dystrophic axons or cell bodies.

In summary, our study provides genetic and molecular evidence for the indispensable role of neuronal autophagy in the maintenance of axonal homeostasis, particularly in local membrane trafficking and turnover. Perturbation of local autophagy in the axons leads to axonopathy. We believe that it is important to study the connection between axonal autophagy impairment and human neuropathological conditions associated with axonal dystrophy.

Materials and Methods

Antibodies. Antibodies used were mouse monoclonal anti-calbindin D-28K (Swant, Bellinzona, Switzerland), anti-calbindin (Sigma, St. Louis, MO), anti-GluRδ2 (BD Transduction Laboratories, San Diego, CA), anti-p62 (American Research Products, Belmont, MA), Cy3-conjugated anti-mouse and anti-rabbit IgG (Upstate Biotechnology, Lake Placid, NY), and NeuN, mGluR1α, and actin antibodies (Chemicon International, Temecula, CA). Anti-Atg7 is described in ref. 19.

Animals. Pcp2-Cre transgenic mice (20) (The Jackson Laboratory, Bar Harbor, ME) and *Atg7*$^{flox/flox}$ mice (19) were crossed to produce *Atg7*$^{flox/flox}$;*Pcp2-Cre* mice. *Atg7*$^{flox/flox}$;*Pcp2-Cre* mice and GFP-LC3 transgenic mice (2) were crossed to produce *Atg7*$^{flox/flox}$;*Pcp2-Cre*/GFP-LC3 mice.

Histological Examination. Mice were fixed by cardiac perfusion with 0.1 M phosphate buffer containing 4% paraformaldehyde. The color images of the Meyer's H&E-stained midsagittal cryosections (10 μm) of cerebella were acquired with a 20× objective lens and a color CCD camera, and later assembled to full images in Photoshop for the quantification of Purkinje cells. Immunofluorescent stained cerebellar samples were prepared as described in ref. 22 and examined by using confocal microscopy.

Behavioral Analyses. Motor function was assessed by the limb-clasping test, rotarod assay, and gait analysis (*SI Materials and Methods*).

Electron Microscopy. Tissue samples were obtained from three *Atg7*$^{flox/flox}$ mice and three *Atg7*$^{flox/flox}$;Pcp2-Cre mice. Details of the experiment are described in *SI Materials and Methods*. In brief, thin sections (70 nm) of the lateral cerebellar nucleus and cerebellar cortex were prepared and examined by transmission electron microscopy (H7500; Hitachi, Tokyo, Japan). A double-blind point-counting method was used to quantify double-membrane vacuole-like structures in 55 micrographs of either *Atg7*$^{flox/flox}$ or *Atg7*$^{flox/flox}$;Pcp2-Cre mice. The total number of these structures overlying at least one intersection of a Photoshop-generated grid was counted to be 52 and 13 for *Atg7*$^{flox/flox}$ and *Atg7*$^{flox/flox}$;Pcp2-Cre samples, respectively. The total number of intersections within these structures was 132 and 19 for *Atg7*$^{flox/flox}$ and *Atg7*$^{flox/flox}$;Pcp2-Cre samples, respectively.

Statistical Analyses. The equality of the variance was first tested by using the F test. Pair-wise comparisons were calculated by using one-tailed Student's t test. The standard error was calculated for each sample.

1. Levine B, Klionsky DJ (2004) *Dev Cell* 6:463–477.
2. Mizushima N, Yamamoto A, Matsui M, Yoshimori T, Ohsumi Y (2004) *Mol Biol Cell* 15:1101–1111.
3. Rubinszstein DC, DiFiglia M, Heintz N, Nixon RA, Qin ZH, Ravikumar B, Stefanis L, Tolkovsky A (2005) *Autophagy* 1:11–22.
4. Yue Z, Horton A, Bravin M, DeJager PL, Selimi F, Heintz N (2002) *Neuron* 35:921–933.
5. Dixon JS (1967) *Nature* 215:657–658.
6. Matthews MR, Raisman G (1972) *Proc R Soc Lond Ser B* 181:43–79.
7. Nixon RA, Wegiel J, Kumar A, Yu WH, Peterhoff C, Cataldo A, Cuervo AM (2005) *J Neuropathol Exp Neurol* 64:113–122.
8. Cataldo AM, Hamilton DJ, Barnett JL, Paskevich PA, Nixon RA (1996) *J Neurosci* 16:186–199.
9. Anglade P, Vyas S, Javoy-Agid F, Herrero MT, Michel PP, Marquez J, Mouatt-Prigent A, Ruberg M, Hirsch EC, Agid Y (1997) *Histol Histopathol* 12:25–31.
10. Roizin L, Stellar S, Willson N, Whittier J, Liu JC (1974) *Trans Am Neurol Assoc* 99:240–243.
11. Sikorska B, Liberski PP, Giraud P, Kopp N, Brown P (2004) *Int J Biochem Cell Biol* 36:2563–2573.
12. Yu WH, Cuervo AM, Kumar A, Peternoff CM, Schmidt SD, Lee JH, Mohan PS, Mercken M, Farmery MR, Tjernberg LO, et al. (2005) *J Cell Biol* 171:87–98.
13. Lin WL, Lewis J, Yen SH, Hutton M, Dickson DW (2003) *J Neurocytol* 32:1091–1105.
14. Li H, Li SH, Yu ZX, Shelbourne P, Li XJ (2001) *J Neurosci* 21:8473–8481.
15. Coleman MP, Perry VH (2002) *Trends Neurosci* 25:532–537.
16. Komatsu M, Waguri S, Chiba T, Murata S, Iwata J, Tanida I, Ueno T, Koike M, Uchiyama Y, Kominami E, et al. (2006) *Nature* 441:880–884.
17. Hara T, Nakamura K, Matsui M, Yamamoto A, Nakahara Y, Suzuki-Migishima R, Yokoyama M, Mishima K, Saito I, Okano H, et al. (2006) *Nature* 441:885–889.
18. Ohsumi Y, Mizushima N (2004) *Semin Cell Dev Biol* 15:231–236.
19. Komatsu M, Waguri S, Ueno T, Iwata J, Murata S, Tanida I, Ezaki J, Mizushima N, Ohsumi Y, Uchiyama Y, et al. (2005) *J Cell Biol* 169:425–434.
20. Barski JJ, Dethleffsen K, Meyer M (2000) *Genesis* 28:93–98.
21. Kabeya Y, Mizushima N, Ueno T, Yamamoto A, Kirisako T, Noda T, Kominami E, Ohsumi Y, Yoshimori T (2000) *EMBO J* 19:5720–5728.
22. Wang QJ, Ding Y, Kohtz S, Mizushima N, Cristea IM, Rout MP, Chait BT, Zhong Y, Heintz N, Yue Z (2006) *J Neurosci* 26:8057–8068.
23. Bjorkoy G, Lamark T, Brech A, Outzen H, Perander M, Overvatn A, Stenmark H, Johansen T (2005) *J Cell Biol* 171:603–614.
24. Banno T, Kohno K (1998) *J Comp Neurol* 402:252–263.
25. Zhang P, Land W, Lee S, Juliani J, Lefman J, Smith SR, Germain D, Kessel M, Leapman R, Rouault TA, et al. (2005) *J Struct Biol* 150:144–153.
26. Eddleman CS, Ballinger ML, Smyers ME, Fishman HM, Bittner GD (1998) *J Neurosci* 18:4029–4041.
27. Li YC, Li YN, Cheng CX, Sakamoto H, Kawate T, Shimada O, Atsumi S (2005) *Neurosci Res* 53:298–303.
28. Coleman M (2005) *Nat Rev Neurosci* 6:889–898.
29. Broadwell RD, Cataldo AM (1984) *J Comp Neurol* 230:231–248.
30. Hollenbeck PJ (1993) *J Cell Biol* 121:305–315.
31. Hosokawa N, Hara Y, Mizushima N (2006) *FEBS Lett* 580:2623–2629.